Journal of Medicinal Chemistry

Article

Development of a 18F-labeled radiotracer with improved brain kinetics for positron emission tomography imaging of translocator protein (18 kDa) in ischemic brain and glioma

Masayuki Fujinaga, Rui Luo, Katsushi Kumata, Yiding Zhang, Akiko Hatori, Tomoteru Yamasaki, Lin Xie, Wakana Mori, Yusuke Kurihara, Masanao Ogawa, Nobuki Nengaki, Feng Wang, and Ming-Rong Zhang

J. Med. Chem., **Just Accepted Manuscript** • Publication Date (Web): 19 Apr 2017

ACS Publications

Journal of Medicinal Chemistry is published by the American Chemical Society. 1155 Sixteenth Street N.W., Washington, DC 20036

Development of a ^{18}F-Labeled Radiotracer with Improved Brain Kinetics for Positron Emission Tomography Imaging of Translocator Protein (18 kDa) in Ischemic Brain and Glioma

Masayuki Fujinaga[†,§], Rui Luo[‡,§], Katsushi Kumata[†,§], Yiding Zhang[†], Akiko Hatori[†], Tomoteru Yamasaki[†], Lin Xie[†], Wakana Mori[†], Yusuke Kurihara[†,¶], Masanao Ogawa[†,¶], Nobuki Nengaki[†,¶], Feng Wang[‡,*], and Ming-Rong Zhang[†,*]

[†]Department of Radiopharmaceuticals Development, National Institute of Radiological Sciences, National Institutes for Quantum and Radiological Science and Technology, 4-9-1 Anagawa, Inage-ku, Chiba 263-8555, Japan.

[‡]Department of Nuclear Medicine, Nanjing First Hospital, Affiliated to Nanjing Medical University, 68 Chanle Road, Nanjing 210006, China.

[¶]SHI Accelerator Service Co., 1-17-6 Osaki, Shinagawa-ku, Tokyo 141-0032, Japan.

[§]These authors contributed equally to this work.

*Corresponding authors.

ABSTRACT

We designed four novel acetamidobenzoxazolone compounds **7a**–**d** as candidates for positron emission tomography (PET) radiotracers for imaging the translocator protein (18 kDa, TSPO) in ischemic brain and glioma. Among these compounds, 2-(5-(6-fluoropyridin-3-yl)-2-oxobenzo[*d*]oxazol-3(2*H*)-yl)-*N*-methyl-*N*-phenylacetamide (**7d**) exhibited high binding affinity (K_i = 13.4 nM) with the TSPO and moderate lipophilicity (LogD: 1.92). [^{18}F]**7d** was radiosynthesized by [^{18}F]fluorination of the bromopyridine precursor **7h** with [^{18}F]F$^-$ in 12 ± 5% radiochemical yield (n = 6, decay-corrected). In vitro autoradiography and PET studies of ischemic rat brain revealed higher binding of [^{18}F]**7d** with TSPO on the ipsilateral side as compared to the contralateral side, and improved brain kinetics than our previously developed radiotracers. Metabolite study of [^{18}F]**7d** showed 93% of unchanged form in the ischemic brain at 30 min after injection. Moreover, PET study with [^{18}F]**7d** provided a clear tumor image in a glioma-bearing rat model. We demonstrated that [^{18}F]**7d** is a useful PET radiotracer for visualizing not only neuroinflammation but also glioma and will translate this radiotracer to a "first-in-human" study in our facility.

INTRODUCTION

Translocator protein (TSPO) is an 18-kDa outer mitochondrial membrane protein that regulates numerous cellular processes including cholesterol, porphyrin, heme, and anion transport; steroid hormone synthesis; apoptosis; cell proliferation; mitochondrial function; immunomodulation; and inflammation.[1] Under normal physiological conditions, TSPO is highly expressed in steroid-producing and mitochondria-enriched tissues such as myocardium, renal tissue, and skeletal muscle, whereas tissues such as brain and liver have relatively low expression.[1] Elevated TSPO expression is implicated in many inflammatory diseases[2] and neuroinflammation[3-7] as well as in various malignancies including glioma,[8-10] astrocytoma,[11] breast cancer,[12] colorectal cancer,[13] and hepatoma[14]. In some TSPO-overexpressing tumor cells, TSPO mediates cholesterol transport into the nucleus, which has been linked to cell proliferation.[15]

A large number of positron emission tomography (PET) studies have visualized TSPO in neuroinflammation,[16-20] peripheral inflammatory diseases,[21-23] and cancer[24-28]. Many PET studies used TPSO-specific radiotracers to monitor activated microglia, which overexpress TSPO during neuroinflammation.[17-20,29-32] In fact, TSPO is associated with pathological conditions such as Alzheimer's and Parkinson's diseases that involve neuroinflammation.[31-35] In addition to neuroinflammation imaging, TSPO expression is also emerging as an important prognostic biomarker in oncology, suggests the imaging utility of TSPO-PET for tumor detection and diagnosis.[13-15,24-28]

The first PET tracer for TSPO, 1-(2-chlorophenyl)-*N*-[^{11}C]methyl-*N*-(1-methylpropyl)-3-isoquinolinecarboxamide ([^{11}C]PK 11195, [^{11}C]**1**) (Figure 1)[36] was used to detect glioblastoma in a patient.[37] PET studies with [^{11}C]**1** were widely used to visualize Alzheimer's disease and other neurodegenerative diseases.[30-32,38,39] However, [^{11}C]**1** has several limitations including relatively low brain

uptake, high non-specific binding, high lipophilicity, and an unfavourable metabolic profile for PET imaging.[39] For instance, quantitation of [^{11}C]**1** was made difficult by a low signal-to-noise ratio, which was likely due to relatively high level of non-specific binding in vivo.[38]

Several dozen ^{11}C and ^{18}F-labeled tracers have been developed for precise visualization of TSPO in inflammatory diseases and tumors by PET.[39-45] The clinically used TSPO PET tracers (Figure 1) mainly include: *N*-(2-[^{11}C],5-dimethoxybenzyl)-*N*-(5-fluoro-2-phenoxyphenyl)acetamide ([^{11}C]DAA1106, [^{11}C]**2a**),[46,47] *N*-(5-fluoro-2-phenoxyphenyl)-*N*-(2-[^{18}F]fluoroethoxy-5-methoxybenzyl)acetamide ([^{18}F]FEDAA1106, [^{18}F]**2b**),[48] *N*-(2-[^{11}C]methoxybenzyl)-*N*-(4-phenoxypyridin-3-yl)acetamide ([^{11}C]PBR28, [^{11}C]**2c**),[49] *N*-[^{18}F]fluoroacetyl-N-(2,5-dimethoxybenzyl)-2-phenoxyaniline ([^{18}F]PBR06, [^{11}C]**2d**),[50] *N*,*N*-diethyl-2-[2-(4-[^{11}C]methoxyphenyl)-5,7-dimethylpyrazolo[1,5-*a*]pyrimidin-3-yl]acetamide ([^{11}C]DPA-713, [^{11}C]**3a**),[51] *N*,*N*-diethyl-2-[2-(4-[^{18}F]fluoroethoxyphenyl)-5,7-dimethylpyrazolo[1,5-*a*]pyrimidin-3-yl]acetamide ([^{18}F]DPA-714, [^{18}F]**3b**),[52] *N*-benzyl-*N*-ethyl-2-(7,8-dihydro-7-[^{11}C]methyl-8-oxo-2-phenyl-9*H*-purin-9-yl)acetamide ([^{11}C]AC-5216, [^{11}C]**4a**),[53] *N*-benzyl-*N*-methyl-2-(7,8-dihydro-7-[^{18}F]fluoroethyl-8-oxo-2-phenyl-9*H*-purin-9-yl)acetamide ([^{18}F]FEDAC, [^{18}F]**4b**),[54] 2-(6-chloro-2-(4-(3-[^{18}F]fluoropropoxy)phenyl)imidazo[1,2-*a*]pyridin-3-yl)-*N*,*N*-diethylacetamide ([^{18}F]PBR111, [^{18}F]**5a**),[55,56] *N*,*N*-di-*n*-propyl-2-[2-(4-[^{11}C]methoxyphenyl)-6,8-dichloroimidazol[1,2-*a*]pyridine-3-yl]acetamide ([^{11}C]CB184, [^{11}C]**5b**),[57] (*S*)-*N*,*N*-diethyl-9-(2-[^{18}F]fluoroethyl)-5-methoxy-2,3,4,9-tetrahydro-1*H*-carbazole-4-carboxamide ([^{18}F]GE-180, [^{18}F]**5c**),[58] and (*R*)-*N*-*sec*-butyl-4-(2-chlorophenyl)-*N*-[^{11}C]methylquinazoline-2-carboxamide ([^{11}C]ER176, [^{11}C]**5d**)[59,60]. Most of these radiotracers bind to TSPO with high in vitro affinity and have higher signal-to-noise ratios

than [^{11}C]**1** in small animals; however, they often exhibit low in vivo specific binding and slow brain kinetics in human brain. Moreover, PET with certain radiotracers such as [^{11}C]**2c** showed variable binding potential among individuals: high-affinity binders, low-affinity binders, and those with mixed-affinities.[61,62] On the other hand, in tumor, particularly glioma imaging studies, challenging points were observed with some radiotracers such as [^{18}F]**3b**. This radiotracer showed a definite level of non-specific uptake accumulation in normal brain due to metabolism, which prevented detection of glioma with modest TSPO expression. [25,26]

Figure 1

We recently reported the development of a new PET tracer, 2-[5-(4-[^{11}C]methoxyphenyl)-2-oxo-1,3-benzoxazol-3(2*H*)-yl]-*N*-methyl-*N*-phenylacetamide ([^{11}C]MBMP, [^{11}C]**6a**) (Figure 2), and its [^{18}F]fluoroethyl derivative ([^{18}F]FEBMP, [^{18}F]**6b**) for imaging TSPO in the brain.[63-65] Both radiotracers, which are acetamidobenzoxazolone analogs, showed high in vitro and in vivo specific bindings with TSPO in the ischemic rat brains. Furthermore, in vitro autoradiography on postmortem human brains demonstrated that [^{18}F]**6b** binding sites were unaffected by TSPO rs6971 and exhibited similar response for TSPO in "binder" and "non-binder" brain sections.[65] However, like many TSPO radiotracers, [^{11}C]**6a** and [^{18}F]**6b** had slow brain kinetics, without significant decreases in radioactivity during the PET scan.[63,65] This was partly attributed to the high lipophilicity (LogD: 3.4 and 3.4) and potent binding affinity (K_i: 3.9 nM and 6.6 nM for TSPO)[64] of **6a** and **6b**. Moreover, radiolabeled metabolites (> 20% of total radioactivity) of [^{11}C]**6a** and [^{18}F]**6b** were detected in the brain, which limits the applicability of these tracers in humans.

In this study, we designed four new acetamidobenzoxazolone analogs ([^{11}C]**7a**–**c** and [^{18}F]**7d**) using [^{11}C]**6a** as the lead compound (Figure 2) and investigated their potential as PET tracers for in vivo imaging of TSPO. We evaluated whether these tracers were superior to [^{11}C]**1**, [^{11}C]**6a**, and [^{18}F]**6b** in terms of brain kinetics and in vivo metabolism and

performed PET studies for visualization of TSPO not only in ischemic brain but also in glioma. A pyridine ring was introduced into [^{11}C]**7a**–**c** and [^{18}F]**7d** in place of the benzene ring in [^{11}C]**6a**. This structural change could decrease their lipophilicity, and we therefore expected these radiotracers to show more rapid brain kinetics and reduced non-specific binding in target tissues. We also predicted that [^{18}F]**7d** would exhibit improved metabolism since the radiolabeling position was different from those in [^{11}C]**6a** and [^{11}C]**7a**–**c**. Moreover, the longer half-life of ^{18}F (110 min *vs.* 20 min for ^{11}C) would allow time for transportation to distant research and clinical facilities.

Figure 2

Here, we report: 1) chemical synthesis of novel unlabeled compounds **7a**–**d**; 2) radiosynthesis of [^{11}C]**7a**–**c** and [^{18}F]**7d**; 3) in vitro binding affinity with TSPO and lipophilicity; 4) in vitro and in vivo specific binding for TSPO and kinetics in the ischemic rat brain when used for autoradiography and PET; 5) metabolite analysis of [^{11}C]**7c** and [^{18}F]**7d** in the plasma and ischemic rat brain; and 6) visualization of glioma in rat brain by PET using [^{18}F]**7d**.

RESULTS AND DISCUSSION

Chemistry. Compounds **7a**–**d** and their corresponding precursors **7e**–**h** for radiolabeling were synthesized (Scheme 1). The reaction of bromobenzoxazolone acetic acid **8**[66] with 2-methylaminopyridine, 4-methylaminopyridine, or *N*-methylaniline in the presence of hydroxybenzotriazole (HOBt) and 1-(3-dimethylaminopropyl)-3-ethylcarbodiimide hydrochloride (WSC) produced acetamidobenzoxazolones **9**–**11** with 44–72% yield. The coupling reaction of compound **9** or **10** with phenylboronic acid derivatives in the presence of palladium catalyst produced **7a**, 7**b**, **7e**, or **7f** with 11–62% yield. Compound **11** coupled with pyridinylboronic acid derivatives, giving rise to **7c**, **7d**, or **7g** with 52–70% yield, while

reaction of **11** with 2-bromopyridine-5-boronic acid generated **7h** with 6% yield. Due to the bromo groups separately presented in **11** and the boron reagent, the coupling reaction generated a complex mixture, from which a small amount of **7h** was separated, which was nonetheless sufficient for radiolabeling and evaluation of [^{18}F]**7d**.

Scheme 1

Radiochemistry. Radiosynthesis of [^{11}C]**7a**–**c** was carried out using a home-made automated synthesis system.[46] The labeling agent [^{11}C]methyl iodide ([^{11}C]MeI) was prepared by reducing cyclotron-produced [^{11}C]CO_2 with lithium aluminum hydride, followed by iodination with 57% hydroiodic acid. The resultant [^{11}C]MeI was purified by distillation and trapped in a *N*,*N*-dimethylformamide (DMF) solution of the desmethyl phenol precursors **7e**–**g** and NaOH (Scheme 2). The [^{11}C]methylation of **7e**–**g** with [^{11}C]MeI proceeded efficiently for 5 min at 80 °C. HPLC purification for each reaction mixture produced [^{11}C]**7a**, [^{11}C]**7b**, and [^{11}C]**7c** with radiochemical yields (decay-corrected) of 36 ± 7% (n = 8), 45 ± 6% (n = 6), and 27 ± 7% (n = 22), respectively, based on [^{11}C]CO_2. Starting with 13.0–18.5 GBq of [^{11}C]CO_2, 1.3–3.2 GBq of [^{11}C]**7a**–**c** was produced with 25–31 min ($n \geq 6$ for each product) of synthesis times from the end of bombardment (EOB).

Scheme 2

[^{18}F]**7d** was radiosynthesized using another home-made automated synthesis system.[48] A mixture of the 2-bromopyridine precursor **7h** and dry [^{18}F]F^- in dimethyl sulfoxide (DMSO) was heated at 130 °C for 10 min. After optimizing the HPLC conditions, [^{18}F]**7d** was easily separated from unreacted **7h** and other chemical impurities; 0.60–1.04 GBq of [^{18}F]**7d** was then produced from 8.9 GBq of [^{18}F]F^- over a period of 65 ± 6 min (n = 6) of synthesis times from EOB. The radiochemical yield of [^{18}F]**7d** was 12 ± 5% (n = 6, decay-corrected) based on [^{18}F]F^-.

The identities of the four radioactive products were confirmed by HPLC by co-injecting unlabeled **7a**–**d**. In the final formulated solutions, the radiochemical purity of [^{11}C]**7a**–**c** and [^{18}F]**7d** exceeded 98% and their specific activities were 70–160 (^{11}C) and 360–420 (^{18}F) GBq/μmol, respectively, at the end of synthesis (EOS), as determined by comparing the assayed radioactivity with the mass measured from the carrier UV peak in the HPLC chromatogram. There were no peaks corresponding to precursors **7e**–**h** observed in the HPLC chromatograms of the final products, which also did not show radiolysis at room temperature within 90 min ([^{11}C]**7a**–**c**) and 180 min ([^{18}F]**7d**) after formulation, indicating that they were radiochemically stable within the time frame of at least one PET scan. These analytical results were consistent with our in-house quality specifications of radiopharmaceuticals.

In Vitro Binding Assay. We measured in vitro binding affinity (K_i) of compounds **7a**–**d** for TSPO in rat brain by assaying competitive binding to the TSPO-specific radiotracer [^{11}C]**1** within the concentration range of 0.3 nM to 3 μM.[64] Specific binding was > 80% for all tested compounds; measured K_i values are shown in Table 1. Compounds **7a**, **7c**, and **7d** showed high binding affinity (20.1, 15.5, and 13.4 nM, respectively) for TSPO, although these affinities were weaker than those of **1** (4.4 nM) and **6a** (3.9 nM). As previously reported, a pharmacophore model study showed that TSPO binding requires three hydrophobic groups and a hydrogen bond acceptor group.[66] Substituting a lipophilic benzene ring in **6a** with a hydrophilic pyridine ring thus decreased the affinity of **7a**–**d** for TSPO. In particular, a marked decrease in binding affinity was observed for **7b** due to the replacement of the benzene ring with a 4-pyridinyl ring. This result suggested that the lipophilic property associated with the 4 position of the **6a** benzene ring is critical determinant of TSPO binding affinity. Although **7a**, **7c**, and **7d** had lower affinity for TSPO than **1** and **6a**, we considered that their affinity was sufficient for the purposes of the present imaging study based on our understanding of and experience with TSPO.[67] Moreover, we expected these radiotracers to

show improved brain kinetics in vivo by more readily releasing from TSPO in the brain, than [^{11}C]**1** and [^{11}C]**6a**. On the other hand, compounds **7a**–**d** did not exhibit appreciable binding to central benzodiazepine receptor (K_i > 1 μM).

Table 1

Computation and Measurement of Lipophilicity. The calculated lipophilicity values at pH = 7.4 (cLogD) for [^{11}C]**7a**–**c** and [^{18}F]**7d** ranged from 2.35 to 3.00 (Table 1). These differed from the LogD values (1.92–3.04) measured by the shake flask method.[48,68] All the measured values for [^{11}C]**7a**–**c** and [^{18}F]**7d** are in the range normally considered as suitable PET tracers.[69] The presence of a hydrophilic pyridine ring reduced the lipophilicity, which may reduce non-specific binding by accelerating the clearance of radioactivity from non-target sites.

In Vitro Autoradiography of Ischemic Rat Brain. TSPO is expressed at low levels in normal rat brain; we therefore used a well-characterized ischemic rat brain model[54,70] to evaluate the in vitro and in vivo specific binding of [^{11}C]**7a**–**c** and [^{18}F]**7d** for TSPO. In this model, neuroinflammation accompanied by microglial activation increases TSPO levels in the ischemic areas, such as the cerebral cortex and striatum.[70] Figure 3 shows the in vitro autoradiograms and result of the quantitative analysis of [^{11}C]**7a** (A), [^{11}C]**7b** (B), [^{11}C]**7c** (C), and [^{18}F]**7d** (D) in the ischemic rat brain. In control sections for [^{11}C]**7a**, [^{11}C]**7c**, and [^{18}F]**7d**, radioactivity was higher on the ipsilateral side (arrow) as compared to the contralateral side, whereas no difference was observed between the two sides for [^{11}C]**7b**. The observed differences in radioactivity level between the ipsilateral and contralateral sides for the all radiotracers were abolished by co-incubation with an excess of unlabeled **7a**–**d** or **1**.

Figure 3

Quantitative analyses of the autoradiograms revealed that the averaged concentration (binding) ratios between the ipsilateral and contralateral sides were 12.0 ± 1.0 for [^{11}C]**7a**, 1.2

± 0.1 for [^{11}C]**7b**, 21.6 ± 3.9 for [^{11}C]**7c**, and 29.8 ± 3.1 for [^{18}F]**7d**, respectively. These ratios decreased to approximately 1 in the presence of unlabeled **7a**–**d** or **1**. Co-incubation with **7a**–**d** or **1** reduced binding on the ipsilateral side to < 10% of the control for [^{11}C]**7a**, [^{11}C]**7c**, and [^{18}F]**7d**. These results demonstrate that [^{11}C]**7a**, [^{11}C]**7c**, and [^{18}F]**7d** specifically bind to TSPO in the ischemic rat brain. The low level of specific binding of [^{11}C]**7b** to TSPO was due to its low in vitro binding affinity (K_i = 198 nM; Table 1). Based on these results, we did not further evaluate [^{11}C]**7b** in our in vivo PET imaging studies.

PET Imaging Studies in Ischemic Rat Brains. Figures 4–6 show representative PET images and time-activity curves (TACs) in the ischemic rat brains after the injection of [^{11}C]**7a**, [^{11}C]**7c**, or [^{18}F]**7d**. Higher uptake of radioactivity was observed on the ipsilateral sides, allowing clear visualization of the ischemic areas ([^{11}C]**7a**, Figure 4A; [^{11}C]**7c**, Figure 5A; [^{18}F]**7d**, Figure 6A). The TACs revealed that the maximum uptake of radioactivity on the ipsilateral sides was 1.72 ± 0.08 standardized uptake value (SUV) for [^{11}C]**7a** (Figure 4D), 0.98 ± 0.03 SUV for [^{11}C]**7c** (Figure 5D), and 1.70 ± 0.16 SUV for [^{18}F]**7d** (Figure 6D). A low and constant uptake (0.19–0.40 SUV) was observed on the contralateral sides starting 10 min after each radiotracer injection. At 10–15 min after the injection, uptake ratios between the ipsilateral and contralateral sides reached the maximum values (2.73, 3.55, and 4.20 for [^{11}C]**7a**, [^{11}C]**7c**, and [^{18}F]**7d**, respectively) (Table 2).

Figures 4–6

Table 2

The PET quantitative value of radiotracer bound to receptor is presented as the non-displaceable binding potential (BP_{ND}), which was non-invasively obtained by simplified reference tissue model (SRTM) analysis using the contralateral side as the reference region.[71] The BP_{ND} values of [^{11}C]**7a**, [^{11}C]**7c**, and [^{18}F]**7d** for the ipsilateral sides are shown in Table 2. [^{18}F]**7d** had the highest value (2.33) followed by [^{11}C]**7c** and [^{11}C]**7a** in that order.

We previously carried out a PET analysis with [^{11}C]**1** in the ischemic rat brain under the same experimental conditions as used here.[63] In that study, [^{11}C]**1** uptake was higher on the ipsilateral than that on the contralateral side. Initially, the maximum radioactivity uptake was 1.00 ± 0.04 SUV (n = 4)[63] on the ipsilateral side, and the maximum uptake ratio (1.80) of uptake between the ipsilateral and contralateral sides was observed at 60 min after the injection, with a BP_{ND} value on the ipsilateral side of 1.24 (Table 2).[63]

Displacement studies using unlabeled **7a** (Figure 4B, E), **7c** (Figure 5B, E), **7d** (Figure 6B, E), or **1** (Figure 4C, F; Figure 5C, F; Figure 6C, F) for [^{11}C]**7a**, [^{11}C]**7c**, or [^{18}F]**7d** 10 min after radiotracer injection minimized the difference in signal between the ipsilateral and contralateral sides in PET images. This displacement first produced a transient increase in uptake in the contralateral side, which was due to the flow of radioactivity from the TSPO-enriched peripheral organs, such the heart, lung, and kidney. Despite the transient increase, the radioactivity uptake at 20 min after injection was reduced to a low level. This result would be consistent with the contralateral side having very little specific binding. From 20 min after injection to the end of the PET scans, there was no difference in radioactivity uptake between the two sides, indicating that displacement by unlabeled compounds reduced binding on the ipsilateral side. This provides evidence for high in vivo specific binding of [^{11}C]**7a**, [^{11}C]**7c**, and [^{18}F]**7d** for TSPO in the ischemic brain.

[^{11}C]**7c** and [^{18}F]**7d** showed higher uptake ratios of the ipsilateral to contralateral sides and higher BP_{ND} values than [^{11}C]**1** (Table 2). Moreover, the maximum ratios between the two sides were achieved at 10–15 min after injection for [^{11}C]**7c** and [^{18}F]**7d**, as compared to 60 min for [^{11}C]**1**. We presumed that the moderate binding affinity for TSPO and lipophilicity of [^{11}C]**7c** and [^{18}F]**7d** were the main reasons for their improved brain kinetics relative to [^{11}C]**1**,[63] [^{11}C]**6a**,[63] [^{18}F]**6b**,[65] and other TSPO radiotracers[47,48,53] developed by our group. The improved kinetics is important for quantification of targeted brain receptors by

PET.

Detection of Radiolabeled Metabolites by HPLC. Given the high BP_{ND} values of [^{11}C]**7c** and [^{18}F]**7d** determined in the ischemic brains, we analyzed their metabolites in plasma and ischemic rat brain by radio-HPLC (Figure 7). Over 95% of radioactivity from the samples was recovered in the HPLC analysis. In plasma, the percentage of unchanged [^{11}C]**7c** [retention time (t_R): 8.0 min] rapidly decreased. A polar radiolabeled metabolite (t_R: 2.8 min) was detected in plasma; a radiolabeled metabolite was also detected in the ischemic brain, accounting for 62% of total radioactivity at 30 min after injection. Plasma and brain metabolites had similar t_R values. Co-injection of the two radioactive fractions into an analytic HPLC column yielded a single peak, confirming that there was a single metabolite. This metabolite might enter the brain, making it difficult to quantify TSPO by PET. We therefore did not further evaluate [^{11}C]**7c**.

Figure 7

[^{18}F]**7d** rapidly degraded in plasma; a polar metabolite (t_R: 2.4 min) was detected at 10 and 30 min after injection. In contrast to [^{11}C]**7c**, 95% and 93% of [^{18}F]**7d** (t_R: 4.3 min) in the brain was intact at 10 and 30 min, respectively, indicating that the in vivo metabolic route of [^{18}F]**7d** was different from that of [^{11}C]**7c**. The polar metabolite of [^{18}F]**7d** in the plasma may be unable to penetrate the blood-brain-barrier or, in the affirmative case, may not persist in the brain due to its hydrophilicity, indicating that the in vivo specific binding observed in the ischemic rat brain was attributable to [^{18}F]**7d** itself. Since only trace amounts of the radiolabeled metabolites were present in the brain, we did not confirm its identity.

Biodistribution. We investigated the distribution of [^{18}F]**7d** in bone and in the whole body of normal mice (Table 3). Intravenous injection of [^{18}F]**7d** into mice resulted in a high uptake of radioactivity (71% to 12% injected dose per gram of wet tissue, % ID/g) in the lungs, heart, and kidneys, which are the organs with high TSPO expression. Medium and low

levels of radioactivity were observed in the small intestine, muscle, liver, spleen, and testis, with uptake values from 0.6% ID/g to 2.9% ID/g. The radioactivity concentration in the blood decreased 5 min after injection and remained at a constant level (0.5–0.7% ID/g), possibly due to continuous release of radiolabeled metabolite from the liver or from the enterohepatic circulation. A relatively high initial uptake (1.8% ID/g) was observed in the mouse brain, the target tissue in this study, and the radioactivity level decreased to approximately 15% of the initial peak value 60 min after injection. On the other hand, low bone uptake is a requirement for most useful ^{18}F-labeled radiotracers.[48] During the initial phase after [^{18}F]**7d** injection, relatively low radioactivity (1.2% ID/g) was detected in the thighbones; this value increased to 2.3% ID/g at 15 min (Table 3). By comparison, 30 min after injection of [^{11}C]**7c** into mice, a moderate level (2.0% ID/g) of radioactivity was also observed in the bone (Supplement Table 2). These results indicate that [^{18}F]**7d** does not induce significant defluorination in vivo.

Table 3

PET Imaging Studies in Glioma. To further evaluate the applicability of [^{18}F]**7d** for in vivo visualization of TSPO, we carried out PET using [^{18}F]**7d** to detect glioma in a rat model, in which C6 glioma cells were implanted into the hemisphere of rat brain[24-26]. Previous studies using this model have reported that TSPO expression was upregulated on the tumor side of the brain bearing glioma.[24-26]

Figure 8A shows PET images of glioma-bearing rat brain after injection of [^{18}F]**7d**. A high radioactivity uptake in the brain was detected on the tumor (ipsilateral) side, whereas the contralateral hemisphere showed a low signal. The tumor-selective uptake of [^{18}F]**7d** provided a good imaging contrast of radioactive signals between the ipsilateral and contralateral sides. The radioactivity accumulated steadily in the tumor and was rapidly cleared from the contralateral side (Figure 8C). Using this side as a reference, the BP_{ND} value

of [^{18}F]**7d** on the ipsilateral side was determined to be 2.29 ± 0.79. The maximum uptake ratio between the ipsilateral and contralateral sides was 4.20 ± 1.09, which was observed at 45–50 min after radiotracer injection.

Figure 8

Blocking experiment with **1** at 1 min before [^{18}F]**7d** injection minimized the radioactive signal contrast between the tumor and contralateral sides, as revealed by PET images (Figure 8B) and TACs (Figure 8D). Thus, treatment with **1** reduced the in vivo specific binding of [^{18}F]**7d** in the tumor area, indicating that the radioactivity reflected TSPO overexpression in the glioma.

CONCLUSIONS

In this study, we developed four radiotracers for imaging TSPO in the rat brains. Of these compounds, [^{18}F]**7d** showed the highest in vitro binding affinity for TSPO. In vitro autoradiography experiments demonstrated that [^{18}F]**7d** bound to TSPO with high specificity in the ischemic rat brain. PET study with [^{18}F]**7d** confirmed its distribution and specificity for TSPO in the brain. [^{18}F]**7d** showed superior in vivo brain kinetics than our TSPO radiotracers previously developed and had higher BP_{ND} for TSPO in the ischemic brain than [^{11}C]**1**. In addition, there were no [^{18}F]**7d** metabolites in the brain and no significant uptake of radioactivity in the bone. Moreover, PET with [^{18}F]**7d** enabled visualization of glioma by providing sufficient contrast in the radioactive signals between the tumor and contralateral sides. These results demonstrate that [^{18}F]**7d** is a useful PET tracer not only for imaging of neuroinflammation but also for glioma detection. We are currently performing PET imaging studies with [^{18}F]**7d** to detect other neuroinflammation, peripheral inflammation, and tumors and to determine whether the [^{18}F]**7d** binding site is affected by TSPO rs6971. We will use this new radiotracer in human study at our facility.

EXPERIMENTAL SECTION

All chemicals were purchased from commercial sources. Melting points (mp) were determined using a Yanaco MP-500P micromelting point apparatus (Yanaco New Science, Kyoto, Japan). ^{1}H NMR (300 MHz) spectra were recorded using a JEOL-AL-300 NMR spectrometer (JEOL, Tokyo, Japan) with tetramethylsilane as an internal standard. All chemical shifts (δ) are reported as ppm downfield relative to the TMS signal. Signals are quoted as s (singlet), d (doublet), t (triplet), br (broad), or m (multiplet). High-resolution fast atom bombardment mass spectra (HRMS) were acquired using a JEOL NMS-SX102 102A spectrometer. Radioisotopes ^{18}F and ^{11}C were produced using a CYPRIS HM-18 cyclotron (Sumitomo Heavy Industry, Tokyo, Japan). Silica gel column chromatography was performed with a C-200 gel (70–230 mesh; Wako Pure Chemical Industries, Osaka, Japan). High performance liquid chromatography (HPLC) separation and analysis were performed using a JASCO HPLC system (JASCO, Tokyo, Japan). HPLC analysis was performed with a Capcell Pak C_{18} column (4.6 mm i.d. × 250 mm, Shiseido, Tokyo) or Fluofix 120N column (4.6 mm i.d. × 250 mm, Wako, Tokyo). The chemical purity of compounds **7a**–**h** was ≥ 95% by HPLC analysis. The analytic conditions were as follows: **7a**–**c**, **7f**, and **7g**: 1.0 mL/min, MeCN/H_2O/Et_3N (50/50/0.1); **7d** and **7h**: 1.0 mL/min, MeCN/H_2O/Et_3N (60/40/0.1); **7e**: 1.0 mL/min, MeCN/H_2O/Et_3N (55/45/0.1). Radiochemical purity of [^{11}C]**7a**–**c** and [^{18}F]**7d** was analyzed by HPLC with a detector to monitor radioactivity under the following conditions: [^{11}C]**7a**: 1.0 mL/min, MeCN/H_2O/Et_3N (55/45/0.1); [^{11}C]**7b** and [^{11}C]**7c**: 1.0 mL/min, MeCN/H_2O/Et_3N (50/50/0.1); and [^{18}F]**7d**: 1.0 mL/min, MeOH/H_2O (50/50). Effluent radioactivity in radio-HPLC was monitored with a NaI (Tl) scintillation detector system. Unless otherwise stated, radioactivity was measured with an IGC-3R Curiemeter (Aloka, Tokyo, Japan). For the in vitro binding assay, [^{11}C]PK 11195 ([^{11}C]**1**) was synthesized by

reacting a desmethyl precursor with [^{11}C]MeI according to a previously reported method.[38] The radiochemical purity and specific activity of [^{11}C]**1** were ≥ 98% and in the range of 50−100 GBq/μmol, respectively, at EOS.

Chemical Synthesis

2-(5-(4-Methoxyphenyl)-2-oxobenzo[*d*]oxazol-3(2*H*)-yl)-*N*-methyl-*N*-(pyridin-2-yl)acetamide (7a). A mixture of **9** (362 mg, 1.0 mmol), 4-methoxyphenylboronic acid (182 mg, 1.2 mmol), $Pd(PPh_3)_4$ (80 mg, 0.07 mmol), and 1 M aqueous K_2CO_3 (3 mL, 3.0 mmol) in 1,4-dioxane (25 mL) was heated at 100 °C for 9 h under a N_2 atmosphere. The mixture was poured into brine and extracted with AcOEt. The organic layer was washed with brine, dried over Na_2SO_4, and evaporated under reduced pressure. Column chromatographic separation of the residue on silica gel using hexane/AcOEt (4/1) followed by hexane/AcOEt (2/1) yielded **7a** (238 mg, 61.1%) as a white powder. mp. 135–136 °C. ^{1}H NMR ($CDCl_3$): δ 3.43 (3H, s), 3.85 (3H, s), 4.82 (2H, s), 6.94–6.99 (2H, m), 7.11 (1H, d, *J* = 1.5 Hz), 7.20–7.33 (4H, m), 7.45–7.50 (2H, m), 7.83 (1H, td, *J* = 1.7, 7.9 Hz), 8.50 (1H, dt, *J* = 1.0, 4.0 Hz). HRMS *m*/*z*: 390.1475 (calculated for $C_{22}H_{20}N_3O_4$: 390.1454).

2-(5-(4-Methoxyphenyl)-2-oxobenzo[*d*]oxazol-3(2*H*)-yl)-*N*-methyl-*N*-(pyridin-4-yl)acetamide (7b). A mixture of **10** (362 mg, 1.0 mmol), 4-methoxyphenylboronic acid (182 mg, 1.2 mmol), $Pd(PPh_3)_4$ (80 mg, 0.07 mmol), and 1 M aqueous K_2CO_3 (3 mL, 3.0 mmol) in 1,4-dioxane (25 mL) was heated at 100 °C for 6 h under a N_2 atmosphere. The miture was poured into brine and extracted with AcOEt. The organic layer was washed with brine, dried over Na_2SO_4, and evaporated under reduced pressure. Column chromatographic separation of the residue on silica gel using hexane/AcOEt (3/1) followed by hexane/AcOEt (1/1) yielded **7b** (125 mg, 32.1%) as a white powder. mp. 197–198 °C. ^{1}H NMR ($CDCl_3$): δ 3.37 (3H, s),

3.84 (3H, s), 4.49 (2H, s), 6.94–7.01 (3H, m), 7.23–7.32 (4H, m), 7.44 (2H, d, *J* = 8.8 Hz), 8.73 (2H, d, *J* = 5.9 Hz). HRMS *m*/*z*: 390.1451 (calculated for $C_{22}H_{20}N_3O_4$: 390.1454).

2-(5-(5-Methoxypyridin-3-yl)-2-oxobenzo[*d*]oxazol-3(2*H*)-yl)-*N*-methyl-*N*-phenylacetamide (7c). A mixture of **11** (72 mg, 0.2 mmol), 3-methoxy-5-(4,4,5,5-tetramethyl-1,3,2-dioxaborolan-2-yl)pyridine (47 mg, 0.2 mmol), $PdCl_2$(dppf) (10 mg, 0.012 mmol), and K_2CO_3 (42 mg, 0.3 mmol) in dimethoxyethane (DME)/H_2O (5/1, 6 mL) was heated at 80 °C for 7 h under a N_2 atmosphere. The mixture was poured into brine and extracted with AcOEt. The organic layer was washed with brine, dried over Na_2SO_4, and evaporated under reduced pressure. Column chromatographic separation of the residue on silica gel using CH_2Cl_2 followed by CH_2Cl_2/MeOH (97/3) yielded **7c** (41 mg, 52%) as a pale brown powder. mp. 207–208 °C (decomposition). ^{1}H NMR ($CDCl_3$): δ 3.33 (3H, s), 3.94 (3H, s), 4.73 (2H, s), 7.02 (1H, s), 7.28 (2H, d, *J* = 1.1 Hz), 7.31–7.47 (3H, m), 7.50–7.61 (3H, m), 8.31 (1H, d, *J* = 2.9 Hz), 8.40 (1H, d, *J* = 1.8 Hz). HRMS *m*/*z*: 390.1489 (calculated for $C_{22}H_{20}N_3O_4$: 390.1454).

2-(5-(6-Fluoropyridin-3-yl)-2-oxobenzo[*d*]oxazol-3(2*H*)-yl)-*N*-methyl-*N*-phenylacetamide (7d)

A mixture of **11** (180 mg, 0.5 mmol), 2-fluoropyridine-5-boronic acid (85 mg, 0.6 mmol), $Pd(PPh_3)_4$ (58 mg, 0.05 mmol), and K_2CO_3 (104 mg, 0.75 mmol) in DME/H_2O (3/1, 12 mL) was heated at 100 °C for 4 h under a N_2 atmosphere. The mixture was poured into brine and extracted with AcOEt. The organic layer was washed with brine, dried over Na_2SO_4, and evaporated under reduced pressure. Column chromatographic separation of the residue on silica gel using hexane/AcOEt (1/1) yielded **7d** (132 mg, 70%) as a white powder. mp. 220–222 °C. ^{1}H NMR ($CDCl_3$): δ 3.33 (3H, s), 4.36 (2H, s), 7.00 (1H, s), 7.01 (1H, dd, *J* =

3.3, 8.1 Hz), 7.21–7.29 (2H, m), 7.35 (2H, d, *J* = 7.3 Hz), 7.43–7.55 (3H, m), 7.92 (1H, dt, *J* = 2.9, 8.4 Hz), 8.37 (1H, d, *J* = 1.8 Hz). HRMS *m*/*z*: 378.1295 (calculated for $C_{21}H_{17}O_3N_3F$: 378.1254).

2-(5-(4-Hydroxyphenyl)-2-oxobenzo[*d*]oxazol-3(2*H*)-yl)-*N*-methyl-*N*-(pyridin-2-yl)acetamide (7e). A mixture of **9** (500 mg, 1.38 mmol), 4-(4,4,5,5-tetramethyl-1,3,2-dioxaborolan-2-yl)phenol (365 mg, 1.66 mmol), $PdCl_2$(dppf) (20 mg, 0.024 mmol), and K_2CO_3 (480 mg, 3.45 mmol) in DME/H_2O (10/1, 11 mL) was heated at 80 °C for 8 h under a N_2 atmosphere. The mixture was poured into brine and extracted with AcOEt. The organic layer was washed with brine, dried over Na_2SO_4, and evaporated under reduced pressure. Column chromatographic separation of the residue using silica gel under CH_2Cl_2/MeOH (100/1) followed by CH_2Cl_2/MeOH (97/3) yielded **7e** (320 mg, 61.8%) as a pale brown powder. mp. 209–210 °C. ^{1}H NMR (DMSO-d_6): δ 3.41 (3H, s), 4.95 (2H, s), 6.85 (2H, d, *J* = 8.8 Hz), 7.30–7.38 (3H, m), 7.46–7.52 (3H, m), 7.64 (1H, d, *J* = 8.1 Hz), 7.93 (1H, t, *J* = 7.0 Hz), 8.52 (1H, d, *J* = 3.3 Hz), 9.54 (1H, s). HRMS *m*/*z*: 376.1304 (calculated for $C_{21}H_{18}N_3O_4$: 376.1297).

2-(5-(4-Hydroxyphenyl)-2-oxobenzo[*d*]oxazol-3(2*H*)-yl)-*N*-methyl-*N*-(pyridin-4-yl)acetamide (7f). A mixture of **10** (500 mg, 1.38 mmol), 4-(4,4,5,5-tetramethyl-1,3,2-dioxaborolan-2-yl)phenol (365 mg, 1.66 mmol), $PdCl_2$(dppf) (20 mg, 0.024 mmol), and K_2CO_3 (480 mg, 3.45 mmol) in DME/H_2O (10/1, 11 mL) was heated at 80 °C for 10 h under a N_2 atmosphere. The mixture was poured into water and extracted with AcOEt. The organic layer was washed with brine, dried over Na_2SO_4, and evaporated under reduced pressure. Column chromatographic separation of the residue on silica gel using CH_2Cl_2/MeOH (100/1) followed by CH_2Cl_2/MeOH (97/3) gave **7f** (57.1 mg, 11.0%) as a pale

brown solid. mp. 260–261 °C. ^{1}H NMR (DMSO-d_6): δ 3.40 (3H, s), 4.86 (2H, s), 6.86 (2H, d, J = 8.4 Hz), 7.30–7.39 (2H, m), 7.47–7.57 (5H, m), 8.63 (2H, d, J = 5.9 Hz), 9.55 (1H, s). HRMS m/z: 376.1293 (calculated for $C_{21}H_{18}N_3O_4$: 376.1297).

2-(5-(5-Hydroxypyridin-3-yl)-2-oxobenzo[*d*]oxazol-3(2*H*)-yl)-*N*-methyl-*N*-phenylacetamide (7g). A mixture of **11** (72 mg, 0.2 mmol), 5-(4,4,5,5-tetramethyl-1,3,2-dioxaborolan-2-yl)-3-pyridinol (44 mg, 0.2 mmol), $PdCl_2$(dppf) (10 mg, 0.012 mmol), and K_2CO_3 (61 mg, 0.44 mmol) in DME/H_2O (5/1, 6 mL) was heated at 80 °C for 8 h under a N_2 atmosphere. The reaction mixture was poured into brine and extracted with AcOEt. The organic layer was washed with brine, dried over Na_2SO_4, and evaporated under reduced pressure. Column chromatographic separation of the residue on silica gel using CH_2Cl_2 followed by CH_2Cl_2/MeOH (97/3) yielded **7g** (46 mg, 61%) as a pale brown powder. mp. 222–223 °C (decomposition). ^{1}H NMR (DMSO-d_6): δ 3.21 (3H, s), 4.40 (2H, s), 7.39–7.61 (9H, m), 8.14 (1H, s), 8.35 (1H, s), 10.07 (1H, s). HRMS m/z: 376.1342 (calculated for $C_{21}H_{18}N_3O_4$: 376.1297).

2-(5-(6-Bromopyridin-3-yl)-2-oxobenzo[*d*]oxazol-3(2*H*)-yl)-*N*-methyl-*N*-phenylacetamide (7h). A mixture of **11** (864 mg, 2.4 mmol), 2-bromopyridine-5-boronic acid (585 mg, 2.9 mmol), $PdCl_2$(dppf) (120 mg, 0.14 mmol), and K_2CO_3 (504 mg, 3.6 mmol) in DME/H_2O (5/1, 27 mL) was heated at 80 °C for 5 h under a N_2 atmosphere. The mixture was then poured into brine and extracted with CH_2Cl_2. The organic layer was washed with brine, dried over Na_2SO_4, and evaporated under reduced pressure. Column chromatographic separation of the residue on silica gel using hexane/AcOEt (2/1) yielded **7h** (28 mg, 6%) as a white powder. mp. 239–241 °C. ^{1}H NMR ($CDCl_3$): δ 3.33 (3H, s), 4.37 (2H, s), 6.99 (1H, d, J = 1.5 Hz), 7.23–7.37 (4H, m), 7.46–7.57 (4H, m), 7.70 (1H, dd, J = 2.7, 8.3 Hz), 8.54 (1H, d, J = 1.8

Hz). HRMS *m*/*z*: 438.0450 (calculated for $C_{21}H_{17}O_3N_3Br$: 438.0453).

2-(5-Bromo-2-oxobenzo[*d*]oxazol-3(2*H*)-yl)-*N*-methyl-*N*-(pyridin-2-yl)acetamide (9). A mixture of 5-bromo-2-oxobenzo[*d*]oxazole[66] (**8**, 3.27g, 12.0 mmol), HOBt (1.62 g, 12.0 mmol), 2-methylaminopyridine (1.56 g, 14.4 mmol), and WSC (3.45 g, 18.0 mmol) in DMF (50 mL) was stirred at room temperature for 3 h. After removing DMF under reduced pressure, the residue was combined with saturated $NaHCO_3$ solution and then extracted with AcOEt. The organic layer was washed with brine, dried over $MgSO_4$, and evaporated under reduced pressure. The residue was purified by column chromatography using CH_2Cl_2, yielding **9** (1.94 g, 44.5%) as a colorless solid. mp 180–182 °C. ^{1}H NMR ($CDCl_3$): δ 3.43 (3H, s), 4.78 (2H, s), 7.05–7.13 (2H, m), 7.21–7.29 (3H, m), 7.84 (1H, dt, *J* = 2.0, 7.8 Hz), 8.49 (1H, d, *J* = 4.8 Hz). HRMS *m*/*z*: 362.0117 (calculated for $C_{15}H_{13}N_3O_3Br$: 362.0140).

2-(5-Bromo-2-oxobenzo[*d*]oxazol-3(2*H*)-yl)-*N*-methyl-*N*-(pyridin-4-yl)acetamide (10). A mixture of **8** (3.27g, 12.0 mmol), HOBt (1.62 g, 12.0 mmol), 4-methylaminopyridine (1.56 g, 14.4 mmol), and WSC (3.45 g, 18.0 mmol) in DMF (50 mL) was stirred at room temperature for 18 h. After removing DMF under reduced pressure, the residue was combined with saturated $NaHCO_3$ solution and then extracted with AcOEt. The organic layer was washed with brine, dried over $MgSO_4$, and evaporated under reduced pressure. The residue was purified by column chromatography using CH_2Cl_2, yielding **10** (3.00 g, 69.1%) as a colorless solid. mp. 166–167 °C. ^{1}H NMR ($CDCl_3$): δ 3.38 (3H, s), 4.44 (2H, s), 7.04–7.09 (2H, m), 7.20–7.23 (1H, m), 7.32 (2H, d, *J* = 6.2 Hz), 8.76 (2H, d, *J* = 6.2 Hz). HRMS *m*/*z*: 362.0148 (calculated for $C_{15}H_{13}N_3O_3Br$: 362.0140).

2-(5-Bromo-2-oxobenzo[*d*]oxazol-3(2*H*)-yl)-*N*-methyl-*N*-phenylacetamide (11). A mixture

of **8** (3.48g, 12.6 mmol), HOBt (2.04 g, 15.1 mmol), *N*-methylaniline (1.63 ml, 15.1 mmol), and WSC (3.62 g, 18.9 mmol) in DMF (50 mL) was stirred at room temperature for 18 h. After removal of DMF under reduced pressure, the residue was added to saturated $NaHCO_3$ solution and then extracted with AcOEt. The organic layer was washed with brine, dried over $MgSO_4$, and evaporated under reduced pressure. The residue was purified by column chromatography using CH_2Cl_2, yielding **11** (3.28 g, 72.1%) as a colorless solid. mp. 127–128 °C. ^{1}H NMR ($CDCl_3$): δ 3.32 (3H, s), 3.86 (3H, s), 4.35 (2H, s), 6.96–7.00 (3H, m), 7.19–7.23 (2H, m), 7.34 (2H, d, J = 7.7 Hz), 7.41–7.54 (5H, m). HRMS *m*/*z*: 361.0209 (calculated for $C_{16}H_{14}N_2O_3Br$: 361.0188).

Radiosynthesis

2-(5-(4-[^{11}C]Methoxyphenyl)-2-oxobenzo[*d*]oxazol-3(2*H*)-yl)-*N*-methyl-*N*-(pyridin-2-yl)acetamide ([^{11}C]7a). After irradiation, the cyclotron-produced [^{11}C]CO_2 was bubbled into 0.4 M lithium aluminium hydride in anhydrous tetrahydrofuran (THF, 0.3 mL). After evaporating the THF, the remaining complex was treated with 57% hydroiodic acid (0.3 mL) to obtain [^{11}C]MeI, which was distilled and immediately transferred under N_2 gas flow into a solution of **7e** (1.0 mg, 2.6 μmol) and 0.5 M aqueous NaOH (7 μL) in DMF (300 μL) at –15 to –20 °C. When the radioactivity reached a plateau, the reaction mixture was heated at 80 °C for 5 min. After completion of the reaction, 1.0 mL of the preparative HPLC mobile phase was added into the reaction vial, and then the reaction solution was applied to the HPLC system. HPLC separation was completed using a Capcell Pack C_{18} column (10 mm i.d. × 250 mm) with MeCN/H_2O/Et_3N (50/50/0.1) at 5.0 mL/min. The radioactive fraction corresponding to [^{11}C]**7a** (t_R: 9.0 min) was collected in a sterile flask containing polysorbate 80 (100 μL) and 25% ascorbic acid (100 μL), evaporated to dryness under vacuum, redissolved in 3 mL of sterile normal saline, and passed through a 0.22 μm Millipore filter

(Waters, Milford, MA, USA), yielding 3.2 GBq of [^{11}C]**7a**. The identity of [^{11}C]**7a** (t_R: 8.1 min) was confirmed by analytical HPLC with **7a**. The synthesis time was 28 min from EOB; radiochemical yield (decay-corrected) was 43% based on [^{11}C]CO_2; radiochemical purity was > 99%; and specific activity at EOS was 130 GBq/μmol.

2-(5-(4-[^{11}C]Methoxyphenyl)-2-oxobenzo[*d*]oxazol-3(2*H*)-yl)-*N*-methyl-*N*-(pyridin-4-yl)acetamide ([^{11}C]7b). [^{11}C]MeI was transferred into a solution of **7f** (1.0 mg, 2.7 μmol) and 0.5 M aqueous NaOH (7 μL) in DMF (300 μL) at –15 to –20 °C. The reaction mixture was heated at 80 °C for 5 min. HPLC separation was performed using a Capcell Pack C_{18} column (10 mm i.d. × 250 mm) with MeCN/H_2O/Et_3N (55/45/0.1) at 5.0 mL/min. The radioactive fraction corresponding to [^{11}C]**7b** (t_R: 9.1 min) was collected and treated to obtain 3.1 GBq of [^{11}C]**7b**. The identity of [^{11}C]**7b** (t_R: 7.0 min) was confirmed by analytical HPLC with **7b**. The synthesis time was 30 min from EOB; radiochemical yield (decay-corrected) was 50% based on [^{11}C]CO_2; radiochemical purity was > 99%; and specific activity at EOS was 160 GBq/μmol.

2-(5-(5-[^{11}C]Methoxypyridin-3-yl)-2-oxobenzo[*d*]oxazol-3(2*H*)-yl)-*N*-methyl-*N*-phenylacetamide ([^{11}C]7c). [^{11}C]MeI was transferred into a solution of **7g** (1 mg, 2.7 μmol) and 0.5 M aqueous NaOH (7 μL) in DMF (300 μL) at –15 to –20 °C. The reaction mixture was heated at 80 °C for 5 min. HPLC separation was carried out using a Capcell Pack C_{18} column (10 mm i.d. × 250 mm) with MeCN/H_2O/Et_3N (50/50/0.1) at 5.0 mL/min. The radioactive fraction corresponding to [^{11}C]**7c** (t_R: 8.1 min) was collected and treated to obtain 2.4 GBq of [^{11}C]**7c**. The identity of [^{11}C]**7c** (t_R: 7.6 min) was confirmed by analytical HPLC with **7c**. The synthesis time was 27 min from EOB; radiochemical yield (decay-corrected) was 33% based on [^{11}C]CO_2; radiochemical purity was > 99%; specific activity at EOS was 150 GBq/μmol.

2-(5-(6-[^{18}F]Fluoropyridin-3-yl)-2-oxobenzo[*d*]oxazol-3(2*H*)-yl)-*N*-methyl-*N*-phenylacetamide ([^{18}F]7d). [^{18}F]Fluorine anion ([^{18}F]F$^-$) was produced using a cyclotron by the ^{18}O(p, n)^{18}F reaction on 98 atom % $H_2{}^{18}O$ (Rotem Industries, Arava, Israel), and was separated from $H_2{}^{18}O$ using the Sep-Pak Accell Plus QMA Plus Light cartridge (Waters). The produced [^{18}F]HF was eluted from the cartridge with a mixture of aqueous K_2CO_3 (0.4 mg/0.2 mL) and a solution of 4,7,13,16,21,24-hexaoxa-1,10-diazabicyclo[8,8,8]hexacosane (7.5 mg) in MeCN (0.2 mL), and transferred into a reaction vessel in a hot cell. The [^{18}F]F$^-$ solution was dried at 120 °C for 30 min to remove H_2O and MeCN. A solution of **7h** (1.5 mg, 3.4 μmol) in DMSO (300 μL) was combined with [^{18}F]F$^-$ and heated at 130 °C for 10 min. After completion of the [^{18}F]fluorination reaction, MeOH/50 mM $MeCO_2NH_4$ (6/4, 500 μL) was added into the reaction mixture, which was separated by HPLC using an Atlantis T3 column (10 mm i.d. × 150 mm, Waters) with MeOH/50 mM $MeCO_2NH_4$ (6/4) at 5.0 mL/min. The radioactive fraction corresponding to [^{18}F]**7d** (t_R: 9.3 min) was collected in a sterile flask containing polysorbate 80 (100 μL) and 25% ascorbic acid (100 μL), evaporated to dryness under vacuum, re-dissolved in 3 mL sterile saline, and passed through a 0.22 μm Millipore filter to obtain the final product. The identity of [^{18}F]**7d** (t_R: 7.7 min) was confirmed by analytical HPLC with **7d**. The synthesis time was 65 min from EOB; radiochemical yield (decay-corrected) was 17% based on [^{18}F]F$^-$; radiochemical purity was > 99%; and specific activity at EOS was 420 GBq/μmol.

Computation and Measurement of Lipophilicity. The cLogD values of [^{11}C]**7a**–**c** and [^{18}F]**7d** were determined computationally using ChemDraw software (ChemBioDraw Ultra 12.0; Perkin-Elmer, Waltham, MA, USA). The LogD value was measured by mixing [^{11}C]**7a**–**c** or [^{18}F]**7d** [radiochemical purity: > 99%; about 200,000 counts per minute (cpm)]

with *n*-octanol (3.0 g) and phosphate buffered saline (PBS; 3.0 g, 0.1 M, pH 7.4) in a test tube, which was vortexed for 3 min at room temperature, followed by centrifugation at 3500 *g* for 5 min. An aliquot of 0.65 mL PBS and 0.65 mL *n*-octanol was removed and weighed and its radioactivity was counted with a 1480 Wizard autogamma counter (Perkin-Elmer), respectively. Each sample from the remaining organic layer was removed and repartitioned until a consistent LogD value was obtained. The LogD value was calculated by comparing the ratio of cpm/g of *n*-octanol to that of PBS and is expressed as LogD = Log[cpm/g (*n*-octanol)/cpm/g (PBS)]. All measurements were performed in triplicate.

Animals. Animals were maintained and handled in accordance with the recommendations of the National Institute of Health and institutional guidelines of the National Institute of Radiological Sciences (NIRS). All experiments conducted at NIRS were approved by the Animal Ethics Committee. Male ddY mice (7 weeks old, 32−35 g) and Sprague-Dawley (SD) rats (male, 7 weeks old, 220−240 g) were purchased from Japan SLC (Shizuoka, Japan), and housed under a 12/12-h dark/light cycle under optimal conditions.

In Vitro Assays of TSPO Binding. The TSPO binding assay was performed as previously described.[64] Briefly, four rats were sacrificed by cervical dislocation under 5% (v/v) isoflurane anaesthesia. The brains were quickly removed and homogenized in ice-cold Tris-HCl buffer (50 mM, pH 7.4) containing 120 μM NaCl. The homogenate was centrifuged at 40,000 *g* for 15 min at 4 °C. The supernatant was discarded and then the pellet was resuspended, homogenized, and centrifuged under the same conditions. This procedure was repeated twice. The pellet was resuspended in 50 mM Tris-HCl buffer (pH 7.4) at a concentration of 100 mg original wet tissue per mL and used for binding assays.

Crude mitochondrial preparations (100 μL) were incubated with [^{11}C]**1** (final concentration: 2.5 nM) and various concentrations (0.3 nM–3 μM) of compounds **7a**−**d** and **1** in a total volume of 1 mL Tris-HCl buffer at room temperature for 30 min, and the reaction was terminated by rapid filtration through a Whatman GF/C glass fiber filter pretreated with 0.3% polyethylenimine using an M-24 cell harvester (Brandel; Neuroscience, Tokyo, Japan). The filters were washed three times with 5 mL of ice-cold Tris-HCl buffer (50 mM), and the filter-bound radioactivity was counted using the autogamma counter. Nonspecific binding was examined using a saturating concentration (10 μM) of **1**. The K_i of each compound for TSPO was determined according to following equation:[72]

$$K_i = \frac{IC_{50}}{1 + \frac{[L]}{K_d}}$$

where [L] is the concentration of [^{11}C]**1** (nM). The dissociation constant (K_d) of [^{11}C]**1** for TSPO was obtained by Scatchard plot analysis.

Ischemic Rat Brain Model. Mild focal ischemia was induced by intraluminal occlusion of the middle cerebral artery for 30 min based on the intraluminal thread model.[54,70] Briefly, healthy SD rats were anesthetized with 4% (v/v) isoflurane and maintained under anaesthesia with 1.8% isoflurane. A 4.0-monofilament nylon suture coated with silicon was inserted into the internal carotid artery up to the level of the middle cerebral artery branches (approximately 16−18 mm from the internal carotid artery), and the neck incision was closed with a silk suture; 30 min after rat had regained consciousness from anaesthesia, they were again anesthetized and the filament was carefully removed for reperfusion. Body temperature was monitored and maintained at optimal levels throughout the surgery. Rats were then used for in vitro autoradiography, PET imaging, and metabolite analysis at 7 days after ischemic surgery.

Glioma Rat Model. Fourteen days before PET imaging, healthy male SD rats were stereotactically inoculated in the right hemisphere with 1.0×10^5 C6 glioma cells (American Type Tissue Collection, Manassas, VA, USA) according to a previously described protocol.[24-26]

In Vitro Autoradiography of Ischemic Rat Brain. Coronal sections (20 μm) were prepared from frozen ischemic rat brains using a cryostat (HM560; Carl Zeiss, Jena, Germany). Brain sections were preincubated for 20 min in 50 mM Tris-HCl buffer (pH 7.4), and the sections were then incubated for 30 min at room temperature in fresh buffer containing [^{11}C]**7a**−**c** (16−18 MBq, 1.1−1.3 nM) or [^{18}F]**7d** (1.0 MBq, 0.015 nM). For the inhibition studies, unlabeled **7a**−**d** (10 μM) or **1** (10 μM) was incubated with [^{11}C]**7a**–**c** or [^{18}F]**7d**; brain sections were then washed (3 × 2 min) with cold buffer, dipped in cold distilled water, and dried with cold air. The sections were placed on imaging plates (BAS-MS2025, Fujifilm, Tokyo, Japan), and autoradiograms were analyzed using a BAS5000 bio-imaging system (Fujifilm). The concentrations of radioactivity determined in brain sections are expressed as photo-stimulated luminescence (PSL) per mm^2.

Radiolabeled Metabolite Analysis in Ischemic Rats. Ischemic rats were intravenously injected via the tail vein with [^{11}C]**7c** (52 MBq, 0.7 nmol) or [^{18}F]**7d** (20 MBq, 0.054 nmol) solutions, then sacrificed by cervical dislocation 10 or 30 min later (n = 4 for each point). Blood and whole brain samples were obtained quickly. The blood sample was centrifuged at 15,000 g for 2 min at 4 °C to separate the plasma. The supernatant (0.5 mL) was collected in a test tube containing MeCN (0.5 mL), and the resultant mixture was vortexed for 15 s and then deproteinized by centrifugation at 15,000 g for 2 min. Rat brain was homogenized in ice-cooled MeCN/H_2O (1/1, 2 mL); the homogenate was centrifuged at 15,000 g for 2 min at

4 °C and the supernatant (0.5 mL) was collected, resuspended in MeCN (0.5 mL), and deproteinized by centrifugation at 15,000 *g* for 2 min. An aliquot of the supernatant (0.2–1.0 mL) obtained from the plasma or brain homogenate was injected into an HPLC system with a radioactivity detector and analyzed using a Capcell Pak C_{18} column (4.6 mm i.d. × 250 mm) with MeCN/H_2O/Et_3N (50/50/0.1) at a flow rate of 1.0 mL/min for [^{11}C]**7c**, and MeCN/H_2O/Et_3N (60/40/0.1) at a flow rate of 1.5 mL/min for [^{18}F]**7d**. The percentage ratio of [^{11}C]**7c** (t_R = 7.1–8.0 min) or [^{18}F]**7d** (t_R = 4.2–4.7 min) to total radioactivity (corrected for decay) on the HPLC chromatogram was calculated as % = (peak area for radiotracer/total peak area) × 100.

PET Study and Image Analysis.

Ischemic rat model. PET scan was carried out using a small-animal PET scanner (Siemens Medical Solutions USA, Knoxville, TN, USA), which provides 159 transaxial slices 0.796 mm (center-to-center) apart, a 10 cm transaxial field of view (FOV), and a 12.7 cm axial FOV for imaging.[70] Ischemic rats were anesthetized with 1.5% (v/v) isoflurane during the scan, and their body temperatures were maintained using a 40°C water circulation system (T/Pump TP401; Gaymar Industries, Orchard Park, NY, USA). Rats were intravenously injected via the tail vein with [^{11}C]**7a** (38.7 ± 1.5 MBq/0.52 ± 0.02 nmol), [^{11}C]**7c** (40.0 ± 1.6 MBq/0.54 ± 0.02 nmol), or [^{18}F]**7d** (18.3 ± 1.0 MBq/0.05 ± 0.003 nmol), and a 60-min list-mode emission scan was conducted immediately. The time frame reconstruction was as follows: 1 min × 4 frames, 2 min × 8 frames, and 5 min × 8 frames. For the displacement experiments, unlabeled compounds **7a**, **7c**, **7d** (1 mg/kg), or **1** (3 mg/kg), dissolved in 500 μL of saline containing 10% ethanol and 5% Tween 80, was injected 10 min after PET scans were initiated. Four independent experiments were performed for each group.

PET scan data modeling was performed using three-dimensional sinograms, which were transformed into two-dimensional sinograms by Fourier rebinning. Dynamic image reconstruction was achieved by filtered back-projection using Hanning's filter with a Nyquist cut-off frequency of 0.5 cycles/pixel. PET images were analyzed using ASIPro VM™ (Analysis Tools and System Setup/Diagnostics Tool; Siemens Medical Solutions). The regions of interest were manually placed on ipsilateral and contralateral sides of the striatum with the same area with reference to the template images of nuclear magnetic resonance. The BP_{ND} on the ipsilateral side of the striatum was calculated with SRTM[71] using the contralateral side as the reference region. The model analysis was performed using PMOD version 3.4 image analysis software (PMOD Technologies, Zurich, Switzerland).

Glioma rat model. PET scan was carried out using the same small-animal PET scanner as mentioned above. Glioma-bearing rats were intravenously injected via the tail vein with [^{18}F]**7d** (19.0 ± 0.8 MBq/0.05 ± 0.002 nmol), and a 60-min list-mode emission scan was immediately performed. The time frame reconstruction was as follows: 1 min × 4 frames, 2 min × 8 frames, and 5 min × 8 frames. For the displacement experiments, unlabeled **1** (3 mg/kg), dissolved in 500 μL of saline containing 10% ethanol and 5% Tween 80, was injected via the tail vein 1 min before PET scans were initiated. Four to five independent experiments were performed for each group. PET scan data were modelled as described above. The BP_{ND} on the tumor (ipsilateral side) was calculated with the SRTM using the same area on the contralateral side as the reference region.

Biodistribution Study. Mice were injected via the tail vein with [^{18}F]**7d** (1.0 MBq, 2.7 pmol) and were sacrificed at five time intervals (1, 5, 15, 30, and 60 min). Blood samples were collected from each group (n = 4) and the brain, heart, kidneys, liver, lungs, spleen, small intestine, testis, muscles, and bones (thighbone) were quickly removed and weighed.

The radioactivity level in each tissue was measured with the autogamma counter and is expressed as percentage of the injected dose per gram of wet tissue (% ID/g). Decay correction was taken into account during the radioactivity measurements.

Statistics. All quantitative data are expressed as the mean ± standard deviation (SD). The relationship between the regional outcome parameters under test and retest conditions were estimated using GraphPad Prism 5 software (GraphPad Software, La Jolla, CA, USA).

ASSOCIATED CONTENT

Supporting Information

Purity of compounds **7a**–**h** determined by HPLC; HPLC analytical charts for **7a**–**h**; HPLC separation and analytic charts for [^{11}C]**7a**–**c** and [^{18}F]**7d**; and biodistribution of [^{11}C]**7c** in mice

AUTHOR INFORMATION

Corresponding Authors

Feng Wang, PhD., Department of Nuclear Medicine, Nanjing First Hospital, Affiliated to Nanjing Medical University, 68 Chanle Road, Nanjing 210006, China. Phone: 86-25-52271456; e-mail: fengwangcn@hotmail.com.

Ming-Rong Zhang, PhD., Department of Radiopharmaceuticals Development, National Institute of Radiological Sciences, National Institutes for Quantum and Radiological Science and Technology, 4-9-1 Anagawa, Inage-ku, Chiba 263-8555, Japan. Phone: 81-43-382-3709; fax: 81-43-206-3261; e-mail: zhang.ming-rong@qst.go.jp.

Author Contributions

[§]M.F., R.L., and K.K. contributed equally.

Notes

The authors declare no competing financial interest.

ACKNOWLEDGMENTS

The authors thank the staff at the National Institute of Radiological Sciences for their assistance with the cyclotron operation, radioisotope production, radiosynthesis, and animal experiments.

ABBREVIATIONS USED

BP_{ND}, nondisplaceable binding potential; DME, dimethoxyethane; DMF, *N*,*N*-dimethylformamide; DMSO, dimethyl sulfoxide; EOB, end of bombardment; EOS, end of synthesis; HOBt, hydroxybenzotriazole; % ID/g, percentage of the injected dose per gram of wet tissue; K_i, binding affinity; PET, positron emission tomography; SRTM, simplified reference tissue model; SD, Sprague-Dawley; SUV, standardized uptake value; TAC, time-activity curve; t_R, retention time; TSPO, translocator protein (18 kDa); WSC, 1-(3-dimethylaminopropyl)-3-ethylcarbodiimide hydrochloride.

REFERENCES

(1) Papadopoulos, V.; Baraldi, M.; Guilarte, T. R.; Knudsen, T. B.; Lacapère, J. J.; Lindemann, P.; Norenberg, M. D.; Nutt, D.; Weizman, A.; Zhang, M.-R.; Gavish, M. Translocator protein (18 kDa): new nomenclature for the peripheral-type benzodiazepine

receptor based on its structure and molecular function. *Trends Pharmacol. Sci.* **2006**, *27*, 402–409.

(2) Batarseh, A.; Papadopoulos, V. Regulation of translocator protein 18 kDa expression in health and disease states. *Mol. Cell Endocrinol*. **2010**, *327*, 1–12.

(3) Myers, R.; Manjil, L. G.; Cullen, B. M.; Price, G. W.; Frackowiak, R. S.; Cremer, J. E. Macrophage and astrocyte populations in relation to [^{3}H]PK 11195 binding in rat cerebral cortex following a local ischaemic lesion. *J. Cereb. Blood Flow Metab.* **1991**, *11*, 314–322.

(4) Venneti, S.; Lopresti, B. J.; Wiley, C. A. The peripheral benzodiazepine receptor (Translocator protein 18kDa) in microglia: from pathology to imaging. *Prog. Neurobiol*. **2006**, *80*, 308–322.

(5) Emsley, H. C.; Smith, C. J.; Tyrrell, P. J.; Hopkins, S. J. Inflammation in acute ischemic stroke and its relevance to stroke critical care. *Neurocrit. Care* **2008**, *9*, 125–138.

(6) Rupprecht, R.; Papadopoulos, V.; Rammes, G.; Baghai, T. C.; Fan, J.; Akula, N.; Groyer, G.; Adams, D.; Schumacher, M. Translocator protein (18 kDa) (TSPO) as a therapeutic target for neurological and psychiatric disorders. *Nat. Rev. Drug. Discov.* **2010**, *9*, 971–988.

(7) Heneka, M. T.; Carson, M. J.; El Khoury, J.; Landreth, G. E.; Brosseron, F.; Feinstein, D. L.; Jacobs, A. H.; Wyss-Coray, T.; Vitorica, J.; Ransohoff, R. M.; Herrup, K.; Frautschy, S. A.; Finsen, B.; Brown, G. C.; Verkhratsky, A.; Yamanaka, K.; Koistinaho, J.; Latz, E.; Halle, A.; Petzold, G. C.; Town, T.; Morgan, D.; Shinohara, M. L.; Perry, V. H.; Holmes, C.; Bazan, N. G.; Brooks, D. J.; Hunot, S.; Joseph, B.; Deigendesch, N.; Garaschuk, O.; Boddeke, E.; Dinarello, C. A.; Breitner, J. C.; Cole, G. M.; Golenbock, D. T.; Kummer, M. P. Neuroinflammation in Alzheimer's disease. *Lancet Neurol.* **2015**, *14*, 388–405.

(8) Starosta-Rubinstein, S.; Ciliax, B. J.; Penney, J. B.; McKeever, P.; Young, A. B. Imaging of a glioma using peripheral benzodiazepine receptor ligands. *Proc. Natl. Acad. Sci. USA*. **1987**, *84*, 891–895.

(9) Roncaroli, F.; Su, Z.; Herholz, K.; Gerhard, A.; Turkheimer, F. E. TSPO expression in brain tumours: is TSPO a target for brain tumour imaging? *Clin. Transl. Imaging.* **2016**, *4*, 145–156.

(10) Zinnhardt, B.; Pigeon, H.; Thézé, B.; Viel, T.; Wachsmuth, L.; Fricke, I. B.; Schelhaas, S.; Honold, L.; Schwegmann, K.; Wagner, S.; Faust, A.; Faber, C.; Kuhlmann, M. T.; Hermann, S.; Schäfers, M.; Winkeler, A.; Jacobs, A. H. Combined PET imaging of the inflammatory tumor microenvironment identifies margins of unique radiotracer uptake. *Cancer Res.* **2017**, *77*, 1831–1841.

(11) Miettinen, H.; Kononen, J.; Haapasalo, H.; Helén, P.; Sallinen, P.; Harjuntausta, T.; Helin, H.; Alho, H. Expression of peripheral-type benzodiazepine receptor and diazepam binding inhibitor in human astrocytomas: relationship to cell proliferation. *Cancer Res.* **1995**, *55*, 2691–2695.

(12) Galiegue, S.; Casellas, P.; Kramar, A.; Tinel, N.; Simony-Lafontaine, J. Immunohistochemical assessment of the peripheral benzodiazepine receptor in breast cancer and its relationship with survival. *Clin. Cancer Res*. **2004**, *10*, 2058–2064.

(13) Maaser, K.; Grabowski, P.; Sutter, A. P.; Höpfner, M.; Foss, H. D.; Stein, H.; Berger, G.; Gavish, M.; Zeitz, M.; Scherübl, H. Overexpression of the peripheral benzodiazepine receptor is a relevant prognostic factor in stage III colorectal cancer. *Clin. Cancer Res*. **2002**, *8*, 3205–3209.

(14) Venturini, I.; Zeneroli, M. L.; Corsi, L.; Avallone, R.; Farina, F.; Alho, H.; Baraldi, C.; Ferrarese, C.; Pecora, N.; Frigo, M.; Ardizzone, G.; Arrigo, A.; Pellicci, R.; Baraldi, M. Up-regulation of peripheral benzodiazepine receptor system in hepatocellular carcinoma. *Life Sci*. **1998**, *63*, 1269–1280.

(15) Hardwick, M.; Fertikh, D.; Culty, M.; Li, H.; Vidic, B.; Papadopoulos, V. Peripheral type benzodiazepine receptor (PBR) in human breast cancer: correlation of breast cancer cell

aggressive phenotype with PBR expression, nuclear localization, and PBR-mediated cell proliferation and nuclear transport of cholesterol. *Cancer Res*. **1999**, *59*, 831–842.

(16) Winkeler, A.; Boisgard, R.; Martin, A.; Tavitian, B. Radioisotopic imaging of neuroinflammation. *J. Nucl. Med.* **2010**, *51*, 1–4.

(17) Dupont, A. C.; Largeau, B.; Santiago Ribeiro, M. J.; Guilloteau, D.; Tronel, C.; Arlicot, N. Translocator protein-18 kDa (TSPO) positron emission tomography (PET) imaging and its clinical impact in neurodegenerative diseases. *Int. J. Mol. Sci.* **2017**, *18*, 785.

(18) Cagnin, A.; Rossor, M.; Sampson, E. L.; Mackinnon, T.; Banati, R. B. In vivo detection of microglial activation in frontotemporal dementia. *Ann. Neurol*. **2004**, *56*, 894–897.

(19) Pavese, N.; Gerhard, A.; Tai, Y. F.; Ho, A. K.; Turkheimer, F.; Barker, R. A.; Brooks, D. J.; Piccini, P. Microglial activation correlates with severity in Huntington disease: a clinical and PET study. *Neurology* **2006**, *66*, 1638–1643.

(20) Ouchi, Y.; Yoshikawa, E.; Sekine, Y.; Futatsubashi, M.; Kanno, T.; Ogusu, T.; Torizuka, T. Microglial activation and dopamine terminal loss in early Parkinson's disease. *Ann. Neurol.* **2005**, *57*, 168–175.

(21) Xie, L.; Yui, J.; Hatori, A.; Yamasaki, T.; Yoshida, Y.; Kumata, K.; Kawamura, K.; Zhang, M.-R. Translocator protein (18 kDa), a potent molecular imaging biomarker for noninvasively distinguishing non-alcoholic fatty liver disease. *J. Hepatol.* **2012**, *57*, 1076–1082.

(22) Lamare, F.; Hinz, R.; Gaemperli, O.; Pugliese, F.; Mason, J. C.; Spinks, T.; Camici, P. G.; Rimoldi, O. E. Detection and quantification of large-vessel inflammation with ^{11}C-(*R*)-PK11195 PET/CT. *J. Nucl. Med.* **2001**, *52*, 33–39.

(23) Hatori, A.; Yui, J.; Yamasaki, T.; Xie, L.; Kumata, K.; Fujinaga, M.; Yoshida, Y.; Ogawa, M.; Nengaki, N.; Kawamura, N.; Fukumura, T.; Zhang, M.-R. PET imaging of lung inflammation with [^{18}F]FEDAC, a radioligand for translocator protein (18 kDa). *PLoS ONE*.

2012, *7*, e45065.

(24) Buck, J. R.; McKinley, E. T.; Hight, M. R.; Fu, A.; Tang, D.; Smith, R. A.; Tantawy, M. N.; Peterson, T. E.; Colvin, D.; Ansari, M. A.; Baldwin, R. M.; Zhao, P.; Guleryuz, S.; Manning, H. C. Quantitative, preclinical PET of translocator protein expression in glioma using ^{18}F-*N*-fluoroacetyl-*N*-(2,5-dimethoxybenzyl)-2-phenoxyaniline. *J. Nucl. Med.* **2011**, *52*, 107–114.

(25) Tang, D.; Hight, M. R.; McKinley, E. T.; Fu, A.; Buck, J. R. R.; Smith R. A.; Tantawy, M. N.; Peterson, T. E.; Colvin, D. C.; Ansari, M. S.; Nickels, M.; Manning, H. C. Quantitative preclinical imaging of TSPO expression in glioma using *N*,*N*-diethyl-2-(2-(4-(2-^{18}F-fluoroethoxy)phenyl)-5,7-dimethylpyrazolo[1,5-*a*]pyrimidin-3-yl)acetamide. *J. Nucl. Med*. **2012**, *53*, 287–294.

(26) Tang, D.; McKinley, E. T.; Hight, M. R.; Uddin, M. R.; Harp, J. M.; Fu, A.; Nickels, M. L.; Buck J. R.; Manning, H. C. Synthesis and structure−activity relationships of 5,6,7-substituted pyrazolopyrimidines: discovery of a novel TSPO PET ligand for cancer imaging. *J. Med. Chem*. **2013**, *56*, 3429−3433.

(27) Wu, C.; Yue, X.; Lang, L.; Kiesewetter, D. O.; Li, F.; Zhu, Z.; Niu, G.; Chen, X. Longitudinal PET imaging of muscular inflammation using ^{18}F-DPA-714 and ^{18}F-Alfatide II and differentiation with tumors. *Theranostics* **2014**, *4*, 546−555.

(28) Zheng, J.; Winkeler, A.; Peyronneau, M. A.; Dolle, F.; Boisgard, R. Evaluation of PET imaging performance of the TSPO radioligand [^{18}F]DPA-714 in mouse and rat models of cancer and inflammation. *Mol. Imaging Biol.* **2016**, *18*, 127−134.

(29) Sandiego, C. M.; Gallezot, J. D.; Pittman, B.; Nabulsi, N.; Lim, K.; Lin, S. F.; Matuskey, D.; Lee, J. Y.; O'Connor, K. C.; Huang, Y.; Carson, R. E.; Hannestad, J.; Cosgrove, K. P. Imaging robust microglial activation after lipopolysaccharide administration in humans with PET. *Proc. Natl. Acad. Sci. U. S. A.* **2015**, *112*, 12468−12473.

(30) Gerhard, A.; Schwarz, J.; Myers, R.; Wise, R.; Banati, R. B. Evolution of microglial activation in patients after ischemic stroke: a [^{11}C](*R*)-PK11195 PET study. *Neuroimage* **2005**, *24*, 591−595.

(31) Gerhard, A. TSPO imaging in parkinsonian disorders. *Clin. Transl. Imaging.* **2016**, *4*, 183−190.

(32) Krstic, D.; Knuesel, I. Deciphering the mechanism underlying late-onset Alzheimer disease. *Nat. Rev. Neurol*. **2013**, *9*, 25−34.

(33) Kreisl, W. C.; Lyoo, C. H.; McGwier, M.; Snow, J.; Jenko, K. J.; Kimura, N.; Corona, W.; Morse, C. L.; Zoghbi, S.; Pike, V. W.; McMahon, F. J.; Turner, R. S.; Innis, R. B. In vivo radioligand binding to translocator protein correlates with severity of Alzheimer's disease. *Brain* **2013,** *136*, 2228–2238.

(34) Golla, S. S.; Boellaard, R.; Oikonen, V.; Hoffmann, A.; van Berckel, B. N.; Windhorst, A. D.; Virta, J.; Haaparanta-Solin, M.; Luoto, P.; Savisto, N.; Solin, O.; Valencia, R.; Thiele, A.; Eriksson, J.; Schuit, R. C.; Lammertsma, A. A.; Rinne, J. O. Quantification of [^{18}F]DPA-714 binding in the human brain: initial studies in healthy controls and Alzheimer's disease patients. *J. Cereb. Blood Flow Metab.* **2015**, *35*, 766−772.

(35) Hamelin, L.; Lagarde, J.; Dorothee, G.; Leroy, C.; Labit, M.; Comley, R. A.; de Souza, L. C.; Corne, H.; Dauphinot, L.; Bertoux, M.; Dubois, B.; Gervais, P.; Colliot, O.; Potier, M. C.; Bottlaender, M.; Sarazin, M.; Clinical, I. Early and protective microglial activation in Alzheimer's disease: a prospective study using ^{18}F-DPA-714 PET imaging. *Brain* **2016**, *139*, 1252−1264.

(36) Camsonne, R.; Crouzel, C.; Comar, D.; Maziere, M.; Prenant, C.; Sastre, J.; Moulin, M. A.; Syrota, A. Synthesis of *N*-[^{11}C]-methyl, *N*-(methyl-1-propyl), (chloro-2-phenyl)-1-isoquinoline carboxamide-3 (PK11195): a new ligand for peripheral benzodiazepine receptors. *J. Labelled Comp. Radiopharm.* **1984**, *21*, 985–991.

(37) Pappata, S.; Cornu, P.; Samson, Y.; Prenant, C.; Benavides, J.; Scatton, B.; Crouzel, C.; Hauw, J. J.; Syrota, A. PET study of carbon-11-PK11195 binding to peripheral type benzodiazepine sites in glioblastoma: a case report. *J. Nucl. Med.* **1991**, *32*, 1608–1610.

(38) Kropholler, M. A.; Boellaard, R.; Schuitemaker, A.; van Berckel, B. N.; Luurtsema, G.; Windhorst, A. D.; Lammertsma, A. A. Development of a tracer kinetic plasma input model for (*R*)-[^{11}C]PK11195 brain studies. *J. Cereb. Blood Flow Metab.* **2005**, *25*, 842–851.

(39) Chauveau, F.; Boutin, H.; Van Camp, N.; Dollé, F.; Tavitian, B. Nuclear imaging of neuroinflammation: a comprehensive review of [^{11}C]PK11195 challengers. *Eur. J. Nucl. Med. Mol. Imaging* **2008**, *35*, 2304–2319.

(40) Dolle, F.; Luus, C.; Reynolds, A.; Kassiou, M. Radiolabelled molecules for imaging the translocator protein (18 kDa) using positron emission tomography. *Curr. Med. Chem*. **2009**, *16*, 2899–2923.

(41) Luus, C.; Hanani, R.; Reynolds, A.; Kassiou, M. The development of PET radioligands for imaging the translocator protein (18 kDa): what have we learned? *J. Labelled Comp. Radiopharm*. **2010**, *53*, 501–510.

(42) Damont, A.; Roeda, D.; Dollé, F. The potential of carbon-11 and fluorine-18 chemistry: illustration through the development of positron emission tomography radioligands targeting the translocator protein 18 kDa. *J. Labelled Comp. Radiopharm.* **2013**, *56*, 96–104.

(43) Ory, D.; Celen, S.; Verbruggen, A.; Bormans, G. PET radioligands for in vivo visualization of neuroinflammation. *Curr. Pharm. Des.* **2014**, *20*, 5897–5913.

(44) Brouwer, C.; Jenko, K.; Zoghbi, S. S.; Innis, R. B.; Pike, V. W. Development of *N*-methyl-(2-arylquinolin-4-yl)oxypropanamides as leads to PET radioligands for translocator protein (18 kDa). *J. Med. Chem.* **2014**, *57*, 6240–6251.

(45) Damont, A.; Medran-Navarrete, V.; Cacheux, F.; Kuhnast, B.; Pottier, G.; Bernards, N.; Marguet, F.; Puech, F.; Boisgard, R.; Dolle, F. Novel pyrazolo[1,5-*a*]pyrimidines as

translocator protein 18 kDa (TSPO) ligands: synthesis, in vitro biological evaluation, [^{18}F]-labeling, and in vivo neuroinflammation PET images. *J. Med. Chem.* **2015**, *58*, 7449–7464.

(46) Zhang, M. R.; Kida, T.; Noguchi, J.; Furutsuka, K.; Maeda, J.; Suhara, T.; Suzuki, K. [^{11}C]DAA1106: radiosynthesis and in vivo binding to peripheral benzodiazepine receptors in mouse brain. *Nucl. Med. Biol*. **2003**, *30*, 513–519.

(47) Maeda, J.; Suhara, T.; Zhang, M. R.; Okauchi, T.; Yasuno, F.; Ikoma, Y.; Inaji, M.; Nagai, Y.; Takano, A.; Obayashi, S.; Suzuki, K. Novel peripheral benzodiazepine receptor ligand [^{11}C]DAA1106 for PET: an imaging tool for glial cells in the brain. *Synapse* **2004**, *52*, 283–291.

(48) Zhang, M. R.; Maeda, J.; Ogawa, M.; Noguchi, J.; Ito, T.; Yoshida, Y.; Okauchi, T.; Obayashi, S.; Suhara, T.; Suzuki, K. Development of a new radioligand, *N*-(5-fluoro-2-phenoxyphenyl)-*N*-(2-[^{18}F]fluoroethyl-5-methoxybenzyl)acetamide, for PET imaging of peripheral benzodiazepine receptor in primate brain. *J. Med. Chem*. **2004**, *47*, 2228–2235.

(49) Briard, E.; Zoghbi, S. S.; Imaizumi, M.; Gourley, J. P.; Shetty, H. U.; Hong, J.; Cropley, V.; Fujita, M.; Innis, R. B.; Pike, V. W. Synthesis and evaluation in monkey of two sensitive ^{11}C-labeled aryloxyanilide ligands for imaging brain peripheral benzodiazepine receptors in vivo. *J. Med. Chem*. **2008**, *51*, 17–30.

(50) Briard, E.; Zoghbi, S. S.; Fabrice G. Simeon, F. G.; Imaizumi, M.; Gourley, J. P.; Shetty, H. U.; Lu, S.; Fujita, M.; Innis, R. B.; Pike V. W. Single-step high-yield radiosynthesis and evaluation of a sensitive ^{18}F-labeled ligand for imaging brain peripheral benzodiazepine receptors with PET. *J. Med. Chem*. **2009**, *52*, 688–699.

(51) Chauveau, F.; Van Camp, N.; Dollé, F.; Kuhnast, B.; Hinnen, F.; Damont, A.; Boutin, H.; James, M.; Kassiou, M.; Tavitian, B. Comparative evaluation of the translocator protein

radioligands ^{11}C-DPA-713, ^{18}F-DPA-714, and ^{11}C-PK11195 in a rat model of acute neuroinflammation. *J. Nucl. Med*. **2009**, *50*, 468–476.

(52) James, M. L.; Fulton, R. R.; Vercoullie, J.; Henderson, D. J.; Garreau, L.; Chalon, S.; Dolle, F.; Costa, B.; Guilloteau, D.; Kassiou, M. DPA-714, a new translocator protein-specific ligand: synthesis, radiofluorination, and pharmacologic characterization. *J. Nucl. Med*. **2008**, *49*, 814–822.

(53) Zhang, M. R.; Kumata, K.; Maeda, J.; Yanamoto, K.; Hatori, A.; Okada, M.; Higuchi, M.; Obayashi, S.; Suhara, T.; Suzuki, K. ^{11}C-AC-5216: a novel PET ligand for peripheral benzodiazepine receptors in the primate brain. *J. Nucl. Med.* **2007**, *48*, 1853–1861.

(54) Yui, J.; Maeda, J.; Kumata, K.; Kawamura, K.; Yanamoto, K.; Hatori, A.; Yamasaki, T.; Nengaki, N.; Higuchi, M.; Zhang, M. R. ^{18}F-FEAC and ^{18}F-FEDAC: PET of the monkey brain and imaging of translocator protein (18 kDa) in the infarcted rat brain. *J. Nucl. Med*. **2010**, *51*, 1301–1309.

(55) Fookes, C. J.; Pham, T. Q.; Mattner, F.; Greguric, I.; Loc'h, C.; Liu, X.; Berghofer, P.; Shepherd, R.; Gregoire, M. C.; Katsifis, A. Synthesis and biological evaluation of substituted [^{18}F]imidazo[1,2-*a*]pyridines and [^{18}F]pyrazolo[1,5-*a*]pyrimidines for the study of the peripheral benzodiazepine receptor using positron emission tomography. *J. Med. Chem.* **2008**, *51*, 3700–3712.

(56) Guo, Q.; Colasanti, A.; Owen, D. R.; Onega, M.; Kamalakaran, A.; Bennacef, I.; Matthews, P. M.; Rabiner, E. A.; Turkheimer, F. E.; Gunn, R. N. Quantification of the specific translocator protein signal of ^{18}F-PBR111 in healthy humans: a genetic polymorphism effect on in vivo binding. *J. Nucl. Med*. **2013**, *54*, 1915–1923.

(57) Toyohara, J.; Sakata, M.; Hatano, K.; Yanai, S.; Endo, S.; Ishibashi, K.; Wagatsuma, K.; Ishii, K.; Ishiwata, K. Preclinical and first-in-man studies of [(11)C]CB184 for imaging the 18-kDa translocator protein by positron emission tomography. *Ann. Nucl. Med*. **2016**, *30*,

534–543.

(58) Feeney, C.; Scott, G.; Raffel, J.; Roberts, S.; Coello, C.; Jolly, A.; Searle, G.; Goldstone, A. P.; Brooks, D. J.; Nicholas, R. S.; Trigg, W.; Gunn, R. N.; Sharp, D. J. Kinetic analysis of the translocator protein positron emission tomography ligand [^{18}F]GE-180 in the human brain. *Eur. J. Nucl. Med. Mol. Imaging* **2016**, *43*, 2201–2210.

(59) Zanotti-Fregonara, P.; Zhang, Y.; Jenko, K. J.; Gladding, R. L.; Zoghbi, S. S.; Fujita, M.; Sbardella, G.; Castellano, S.; Taliani, S.; Martini, C.; Innis, R. B.; Da Settimo, F.; Pike, V. W. Synthesis and evaluation of translocator 18 kDa protein (TSPO) positron emission tomography (PET) radioligands with low binding sensitivity to human single nucleotide polymorphism rs6971. *ACS Chem. Neurosci*. **2014**, *5*, 963–971.

(60) Ikawa, M.; Lohith, T. G.; Shrestha, S.; Telu, S.; Zoghbi, S. S.; Castellano, S.; Taliani, S.; Da Settimo, F.; Fujita, M.; Pike, V. W.; Innis, R. B. ^{11}C-ER176, a radioligand for 18-kDa translocator protein (TSPO), has adequate sensitivity to robustly image all three affinity genotypes in human brain. *J. Nucl. Med.* **2017**, *58*, 320–325.

(61) Owen, D. R.; Yeo, A. J.; Gunn, R. N.; Song, K.; Wadsworth, G.; Lewis, A.; Rhodes, C.; Pulford, D. J.; Bennacef, I.; Parker, C. A.; StJean, P. L.; Cardon, L. R.; Mooser, V. E.; Matthews, P. M.; Rabiner, E. A.; Rubio, J. P. An 18-kDa translocator protein (TSPO) polymorphism explains differences in binding affinity of the PET radioligand PBR28. *J. Cereb. Blood Flow Metab.* **2012**, *32*, 1–5.

(62) Yoder, K. K.; Nho, K.; Risacher, S. L.; Kim, S.; Shen, L.; Saykin, A. J. Influence of TSPO genotype on ^{11}C-PBR28 standardized uptake values. *J. Nucl. Med*. **2013**, *54*, 1320–1322.

(63) Tiwari, A. K.; Yui, J.; Fujinaga, M.; Kumata, K.; Shimoda, Y.; Yamasaki, T.; Xie, L.; Hatori, A.; Maeda, J.; Nengaki, N.; Zhang, M. R. Characterization of a novel acetamidobenzoxazolone-based PET ligand for translocator protein (18 kDa) imaging of

neuroinflammation in the brain. *J. Neurochem*. **2014**, *129*, 712–720.

(64) Tiwari, A. K.; Fujinaga, M.; Yui, J.; Yamasaki, T.; Xie, L.; Kumata, K.; Mishra, A. K.; Shimoda, Y.; Hatori, A.; Ji, B.; Ogawa, M.; Kawamura, K.; Wang, F.; Zhang, M. R. Synthesis and evaluation of new ^{18}F-labelled acetamidobenzoxazolone-based radioligands for imaging of the translocator protein (18 kDa, TSPO) in the brain. *Org. Biomol. Chem*. **2014**, *12*, 9621–9630.

(65) Tiwari, A. K.; Ji, B.; Yui, J.; Fujinaga, M.; Yamasaki, T.; Xie, L.; Luo, R.; Shimoda, Y.; Kumata, K.; Zhang, Y.; Hatori, A.; Maeda, J.; Higuchi, M.; Wang, F.; Zhang, M. R. [^{18}F]FEBMP: positron emission tomography imaging of TSPO in a model of neuroinflammation in rats, and in vitro autoradiograms of the human brain. *Theranostics* **2015**, *5*, 961–969.

(66) Fukaya, T.; Kodo, T.; Ishiyama, T.; Kakuyama, H.; Nishikawa, H.; Baba, S.; Masumoto, S. Design, synthesis and structure–activity relationships of novel benzoxazolone derivatives as 18 kDa translocator protein (TSPO) ligands. *Bioorg. Med. Chem*. **2012**, *20*, 5568–5582.

(67) Kumata, K.; Yui, J.; Hatori, A.; Fujinaga, M.; Yanamoto, K.; Yamasaki, T.; Kawamura, K.; Wakizaka, H.; Nengaki, N.; Yoshida, Y.; Ogawa, M.; Fukumura, T.; Zhang, M. R. Synthesis and evaluation of novel carbon-11 labeled oxopurine analogs for positron emission tomography imaging of translocator protein (18 kDa) in peripheral organs. *J. Med. Chem*. **2011**, *54*, 6040–6049.

(68) Zoghbi, S. S.; Anderson, K. B.; Jenko, K. J.; Luckenbaugh, D. A.; Innis, R. B.; Pike, V. W. On quantitative relationships between drug-like compound lipophilicity and plasma free fraction in monkey and human. *J. Pharm. Sci.* **2012**, *101*, 1028–1039.

(69) Pike, V. W. Considerations in the development of reversibly binding PET radioligands for brain imaging. *Curr. Med. Chem.* **2016**, *23*, 1818–1869.

(70) Yui, J.; Hatori, A.; Kawamura, K.; Yanamoto, K.; Yamasaki, T.; Ogawa, M.; Yoshida, Y.; Kumata, K.; Fujinaga, M.; Nengaki, N.; Fukumura, T.; Suzuki, K.; Zhang, M. R. Visualization of early infarction in rat brain after ischemia using a translocator protein (18 kDa) PET ligand [^{11}C]DAC with ultra-high specific activity. *Neuroimage* **2011**, *54*, 123–130.

(71) Lammertsma, A. A.; Hume, S. P. Simplified reference tissue model for PET receptor studies. *Neuroimage* **1996**, *4*, 153–158.

(72) Cheng, Y. C.; Prusoff, W. H. Relationship between inhibition constant (K_i) and the concentration of inhibitor which causes 50 percent inhibition (IC_{50}) of an enzymatic reaction. *Biochem. Pharmaco.* **1973**, *92*, 881–894.

Table 1. In Vitro Binding Affinity (K_i) for TSPO and Lipophilicity

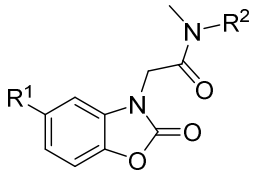

Compound	R^1	R^2	Affinity for TSPO	Lipophilicity	
			K_i (nM)	LogD	cLogD[a]
7a	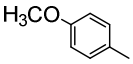		20.1 ± 7.2	3.04	2.69
7b	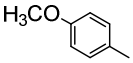		198.4 ± 51.7	2.65	2.69
7c	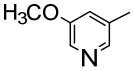		15.5 ± 7.4	2.87	2.35
7d			13.4 ± 5.2	1.92	3.00
6a	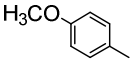		3.9 ± 0.6[b]	3.4[b]	3.3
1 (PK 11195)			4.4 ± 0.4[b]	3.7[b]	5.1

[a]cLogD values were calculated with ChemBioDraw Ultra 12.0. [b]Value was obtained from reference 66

Table 2. Maximum uptake ratio of ipsilateral to contralateral sides and BP_{ND} in the ischemic brain

Radiotracer	Maximum uptake ratio[a] of ipsilateral to contralateral sides	BP_{ND}[a]
[^{11}C]**7a**	2.73 ± 0.26[b]	1.35 ± 0.21
[^{11}C]**7c**	3.55 ± 0.37[b]	1.93 ± 0.15
[^{18}F]**7d**	4.20 ± 0.37[b]	2.33 ± 0.25
[^{11}C]**1**	1.80 ± 0.18[c]	1.24 ± 0.39[d]

[a]Values of ratio and BP_{ND} are the mean ± SD measured in four ischemic rat brains; [b]Achieved at 10-15 min after the radiotracer injection; [c]Achieved at 60 min after the radiotracer injection;[63] [d]Value was obtained from reference 63.

Table 3. Biodistribution for [^{18}F]**7d** in mice

Tissue	1 min	5 min	15 min	30 min	60 min
Blood	1.68 ± 0.11	0.62 ± 0.06	0.68 ± 0.07	0.71 ± 0.07	0.53 ± 0.07
Heart	16.16 ± 0.91	10.03 ± 0.39	5.11 ± 0.66	3.15 ± 0.28	1.97 ± 0.10
Lungs	71.26 ± 6.03	22.75 ± 2.68	12.58 ± 2.30	7.97 ± 0.37	5.62 ± 0.38
Liver	2.87 ± 0.43	5.39 ± 0.78	6.23 ± 0.45	5.70 ± 0.78	3.75 ± 0.34
Spleen	2.41 ± 0.51	6.51 ± 0.74	7.03 ± 0.39	5.68 ± 0.16	3.66 ± 0.17
Kidneys	11.80 ± 1.36	15.25 ± 1.44	13.63 ± 0.94	9.72 ± 0.41	7.62 ± 0.77
Small intestine	4.33 ± 0.16	7.32 ± 1.27	14.16 ± 4.58	18.62 ± 5.01	12.10 ± 3.89
Testis	0.56 ± 0.03	0.82 ± 0.07	1.03 ± 0.10	1.20 ± 0.08	0.96 ± 0.10
Muscle	2.26 ± 0.36	2.22 ± 0.18	1.78 ± 0.17	1.18 ± 0.05	0.95 ± 0.14
Bone	1.21 ± 0.19	2.09 ± 0.13	2.25 ± 0.21	2.11 ± 0.05	1.61 ± 0.23
Brain	1.78 ± 0.07	0.86 ± 0.09	0.52 ± 0.04	0.41 ± 0.01	0.26 ± 0.01

Data are %ID/g tissue (mean ± SD ; n = 4).

Scheme 1. Chemical synthesis of **7a**–**d**[a]

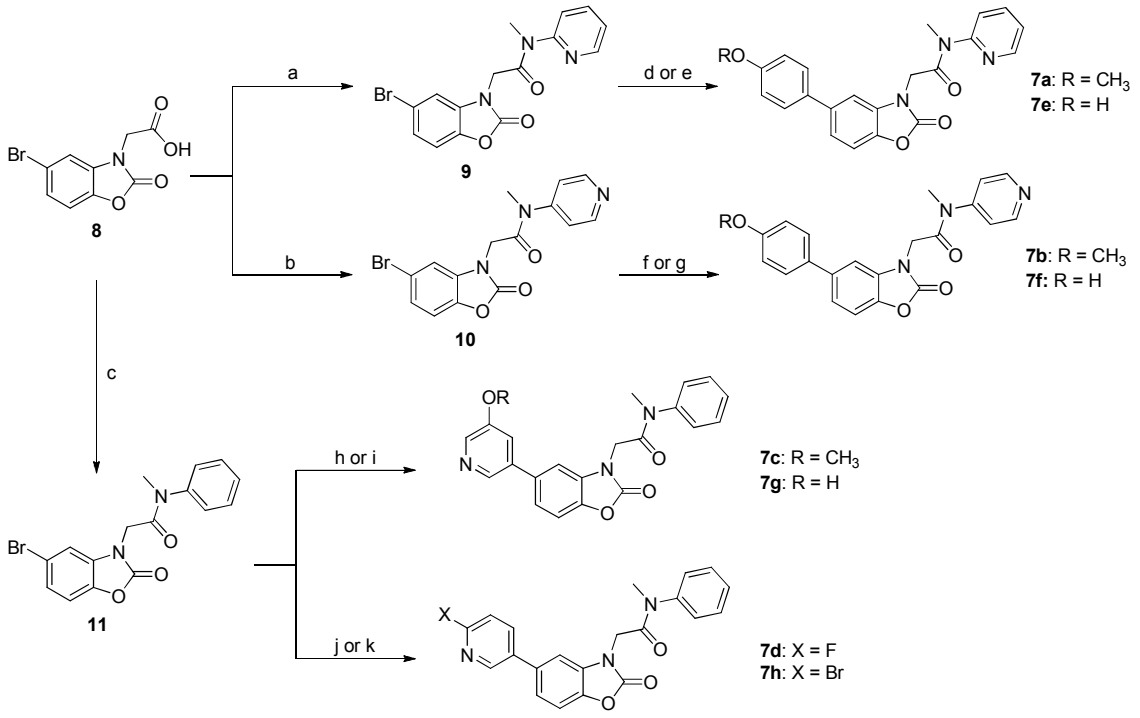

[a]Reagents and conditions: (a)–(c): HOBt, WSC, DMF, room temperature, 3–18 h, 2-methylaminopyridine for **9**, 4-methylaminopyridine for **10**, *N*-methylaniline for **11**; (d) 4-methoxyphenylboronic acid, $Pd(PPh_3)_4$, K_2CO_3, 1,4-dioxane, 100 °C, 9 h; (e) 4-(4,4,5,5-tetramethyl-1,3,2-dioxaborolan-2-yl)phenol, $PdCl_2$(dppf), K_2CO_3, DME/H_2O, 80 °C, 8 h; (f) 4-methoxyphenylboronic acid, $Pd(PPh_3)_4$, K_2CO_3, 1,4-dioxane, 100 °C, 6 h; (g) 4-(4,4,5,5-tetramethyl-1,3,2-dioxaborolan-2-yl)phenol, $PdCl_2$(dppf), K_2CO_3, DME/H_2O,, 80 °C, 10 h; (h) 3-methoxy-5-(4,4,5,5-tetramethyl-1,3,2-dioxaborolan-2-yl)pyridine, $PdCl_2$(dppf), K_2CO_3, DME/H_2O, 80 °C, 7 h; (i) 5-(4,4,5,5-tetramethyl-1,3,2-dioxaborolan-2-yl)-3-pyridinol, $PdCl_2$(dppf), K_2CO_3, DME/H_2O, 80 °C, 8 h; (j) 2-fluoropyridine-5-boronic acid, $Pd(PPh_3)_4$, K_2CO_3, DME/H_2O, 80 °C, 4 h; (k). 2-bromopyridine-5-boronic acid, $PdCl_2$(dppf), K_2CO_3, DME/H_2O, 80 °C, 5 h.

Scheme 2. Radiosynthesis of [^{11}C]**7a**–**c** and [^{18}F]**7d**[a]

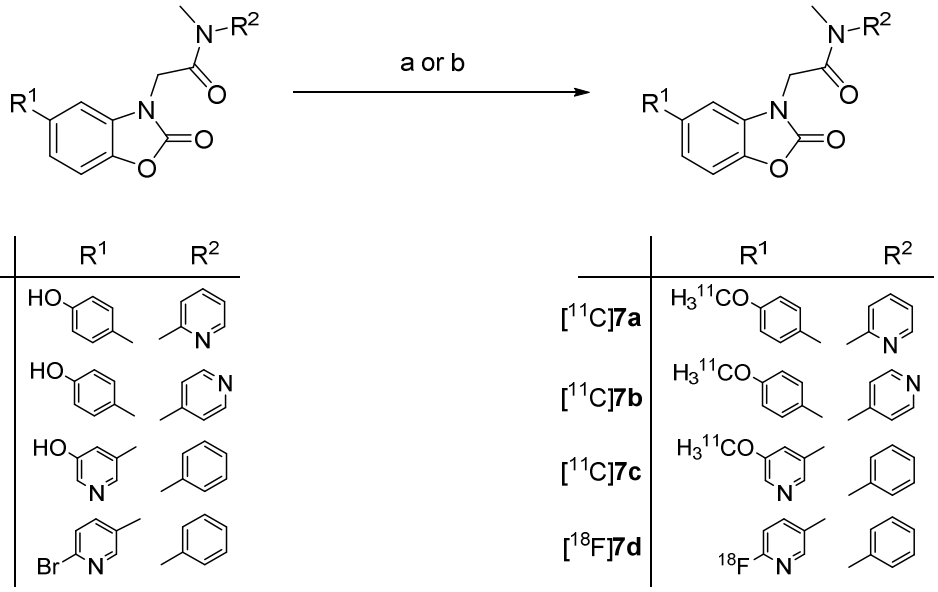

[a]Reagents and conditions: (a) [^{11}C]MeI, NaOH, DMF, 80 °C, 5 min. (b) [^{18}F]KF, 4,7,13,16,21,24-hexaoxa-1,10-diazabicyclo[8,8,8]hexacosane, DMSO, 130 °C, 10 min.

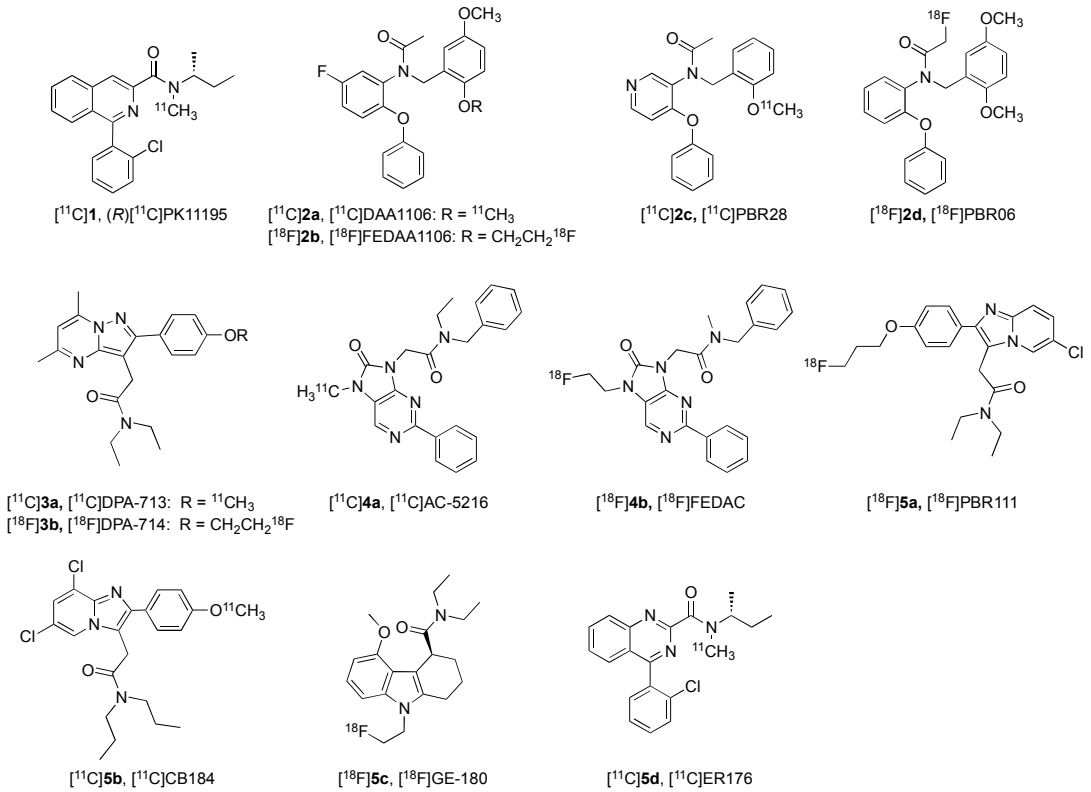

Figure 1. Representative chemical structures of TSPO PET tracers used in human studies.

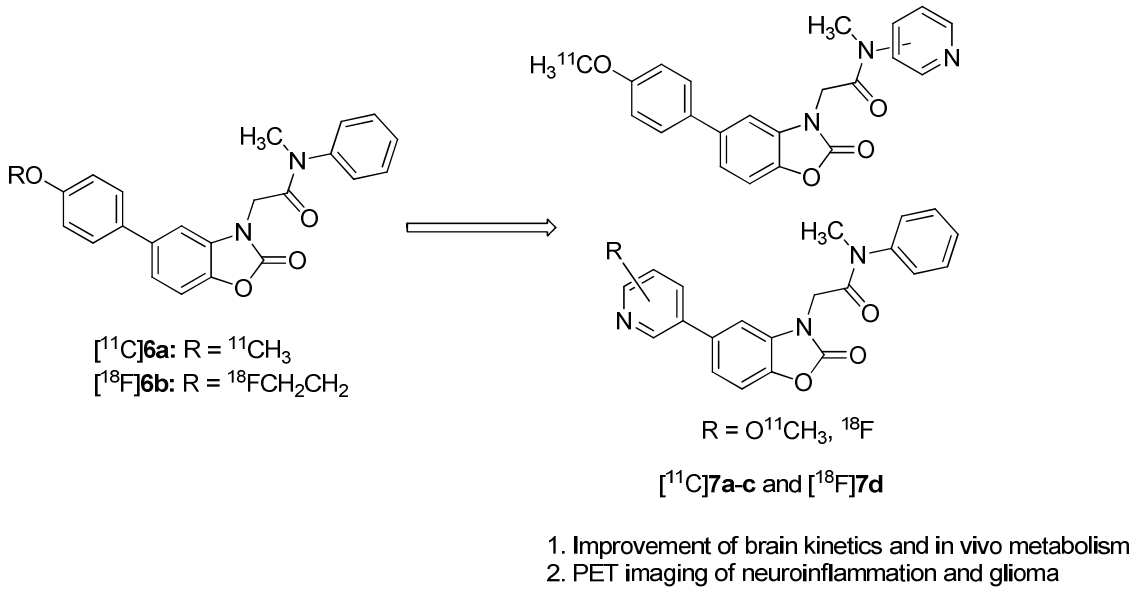

Figure 2. Development of new radiotracers for TSPO using [^{11}C]**6a** as the lead compound.

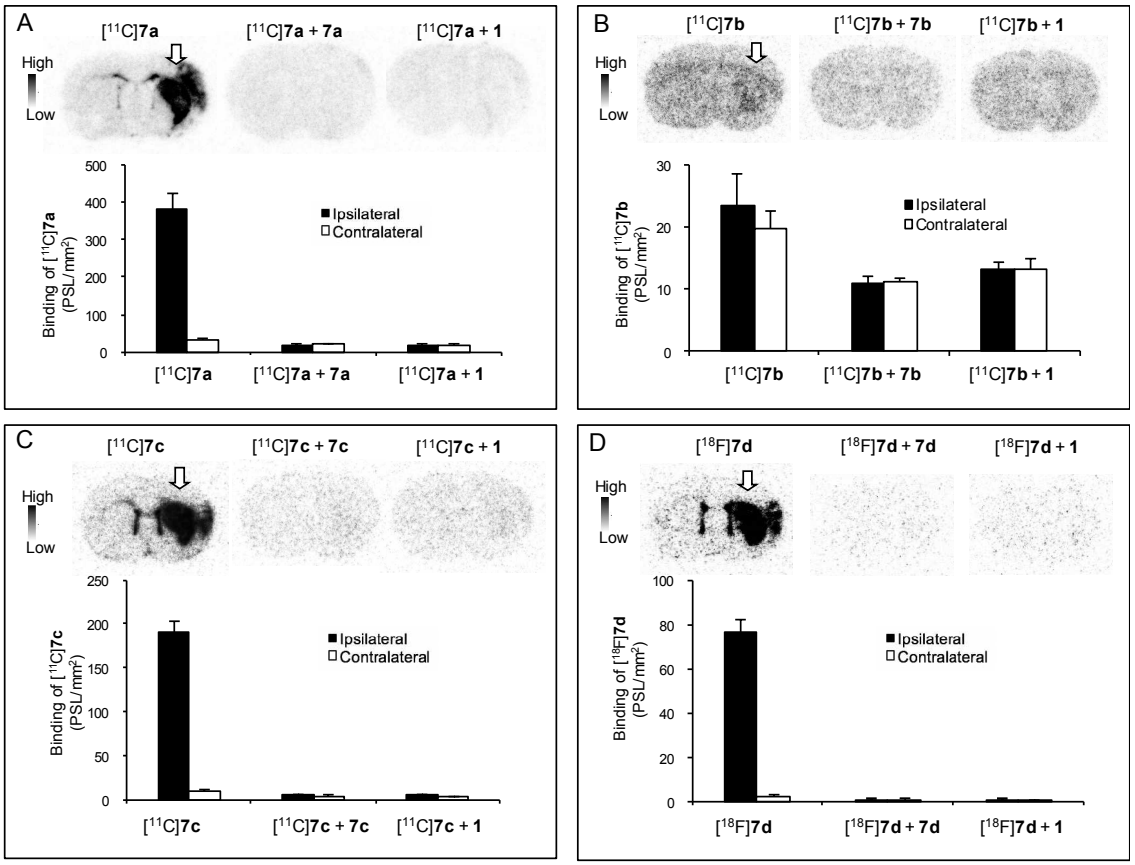

Figure 3. Representative *in vitro* autoradiograms and quantitative analytical results of [^{11}C]**7a–c** and [^{18}F]**7d** in ischemic rat brains (n = 4). Arrows indicate ischemic areas. (A): [^{11}C]**7a**; (B): [^{11}C]**7b**; (C): [^{11}C]**7c**; (D) [^{18}F]**7d**. Specific binding in ischemic brain sections were examined by incubation with unlabeled compounds **7a–d** or **1**. Quantification of autoradiograms was performed for [^{11}C]**7a–c** and [^{18}F]**7d** only and co-incubation of [^{11}C]**7a–c** and [^{18}F]**7d** with unlabeled compounds **7a–d** or **1**. Concentrations of radioactivity in brain regions are expressed as photo-stimulated luminescence (PSL)/mm^2.

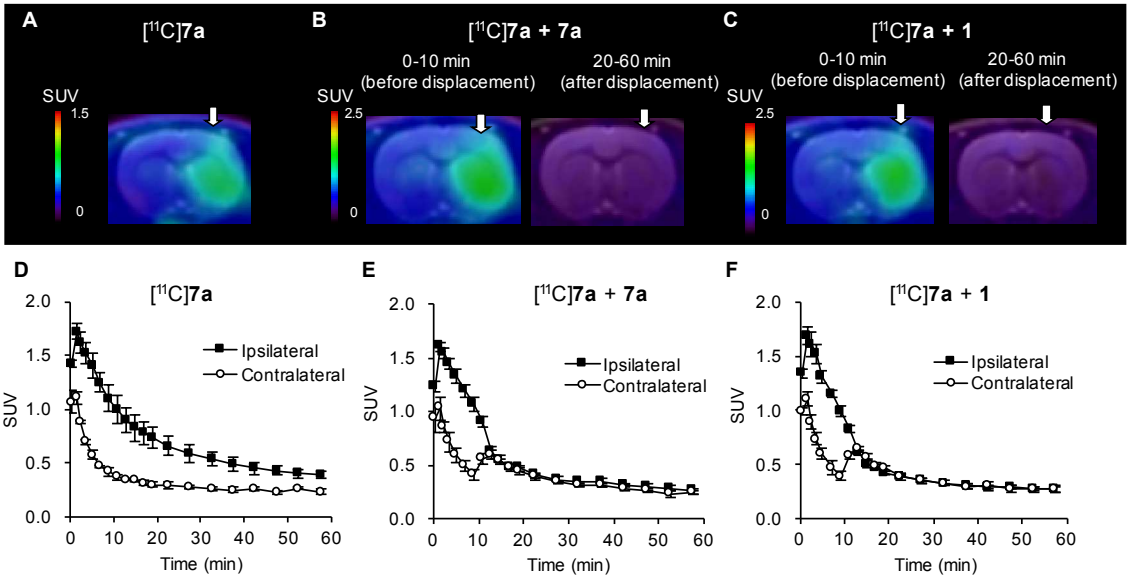

Figure 4. PET imaging with [^{11}C]**7a** in ischemic rat brains. Arrows indicate ischemic areas. (A) and (D): Representative coronal PET images and TACs for ipsilateral and contralateral striatum. (B) and (E): Representative coronal PET images and TACs by displacement with unlabeled **7a** at 10 min following [^{11}C]**7a** injection. (C) and (F): Representative coronal PET images and TACs by displacement with unlabeled **1** at 10 min following [^{11}C]**7a** injection. Data (mean ± SD, n = 4) were obtained from four ischemic rat brains.

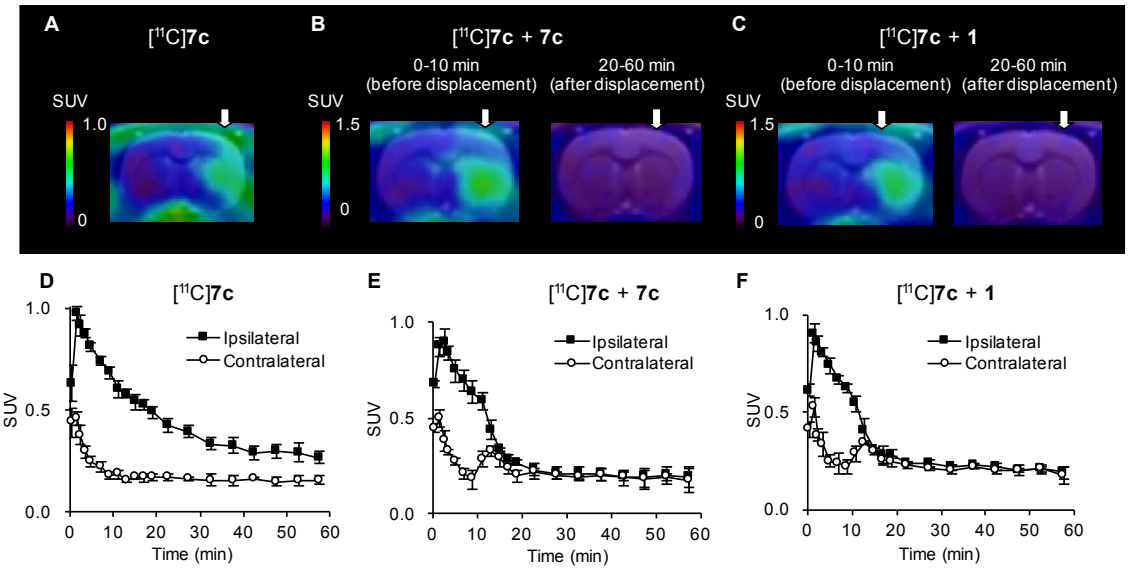

Figure 5. PET imaging with [^{11}C]**7c** in ischemic rat brains. Arrows indicate ischemic areas. (A) and (D): Representative coronal PET images and TACs for ipsilateral and contralateral striatum. (B) and (E): Representative coronal PET images and TACs by displacement with unlabeled **7c** at 10 min following [^{11}C]**7c** injection. (C) and (F): Representative coronal PET images and TACs by displacement with unlabelled **1** at 10 min following [^{11}C]**7c** injection. Data (mean ± SD, n = 4) were obtained from four ischemic rat brains.

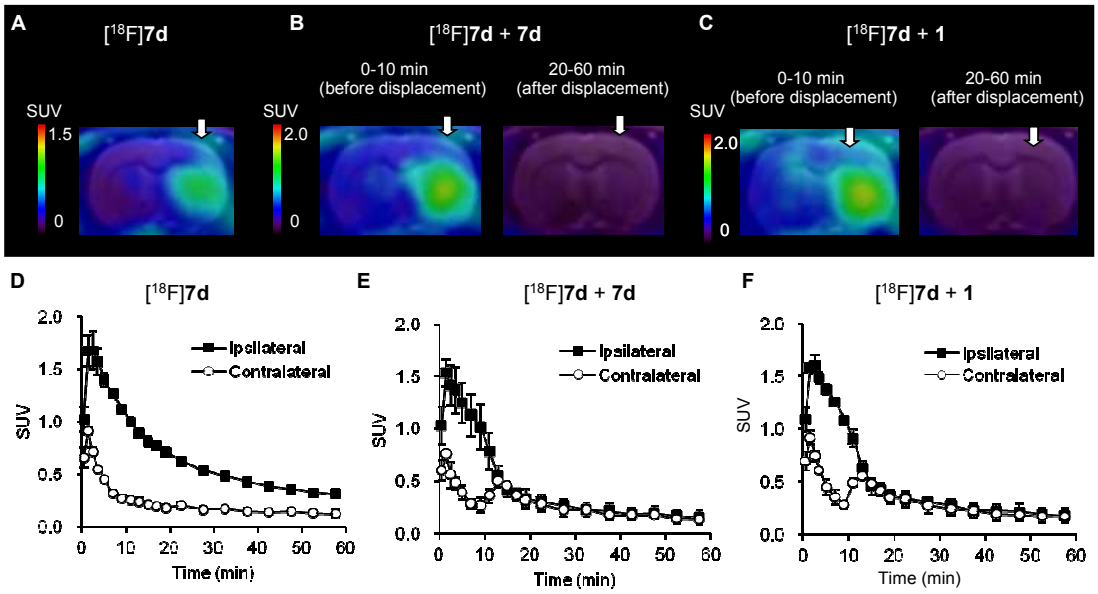

Figure 6. PET imaging with [^{18}F]**7d** in ischemic rat brains. Arrows indicate ischemic areas. (A) and (D): Representative coronal PET image and TACs for ipsilateral and contralateral striatum. (B) and (E): Representative coronal PET images and TACs by displacement with unlabeled **7d** at 10 min following [^{18}F]**7d** injection. (C) and (F): Representative coronal PET images and TACs by displacement with unlabeled **1** at 10 min following [^{18}F]**7d** injection. Data (mean ± SD, n = 4) were obtained from four ischemic rat brains.

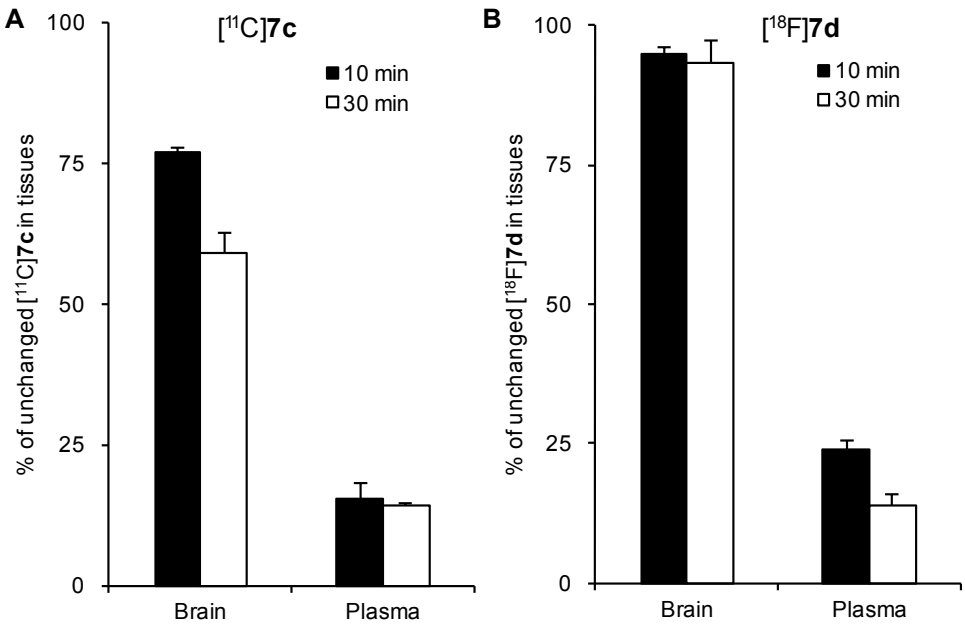

Figure 7. Percentages (means ± SD) of unchanged [^{11}C]**7c** (A) and [^{18}F]**7d** (B) in plasma and brain tissue from rats (n = 4) 10 and 30 min after radiotracer injection.

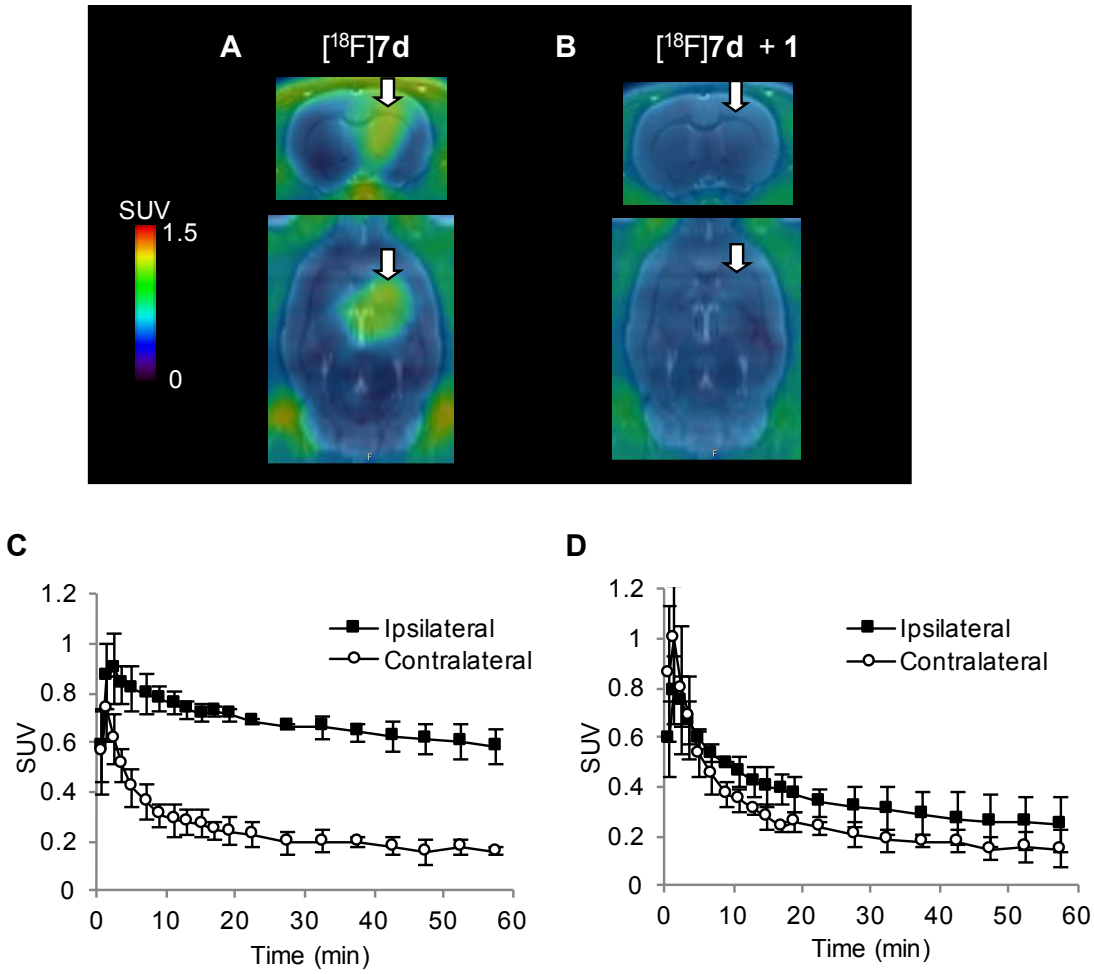

Figure 8. PET imaging with [^{18}F]**7d** in glioma-bearing rat brains. Arrows indicate glioma areas. (A) and (C): Representative coronal and transverse PET images and TACs for ipsilateral and contralateral sides. (B) and (D): Representative coronal and transverse PET images and TACs by treatment with unlabeled **1** at 1 min before [^{18}F]**7d** bolus injection. Data (mean ± SD, n = 4) were obtained from four glioma-bearing rat brains.

Table of Content Graphic

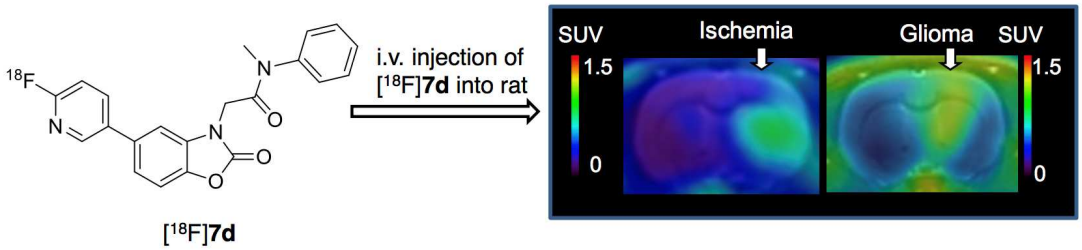

[18F]**7d**